Title
Influence of Tundra Polygon Type and Climate Variability on CO2 and CH4 Fluxes Near Utqiagvik, Alaska

Journal
Journal of Geophysical Research Biogeosciences, 126(12)

ISSN
2169-8953

Authors
Dengel, Sigrid
Billesbach, Dave
Torn, Margaret S

Publication Date
2021-12-01

DOI
10.1029/2021jg006262

Peer reviewed

JGR Biogeosciences

RESEARCH ARTICLE
10.1029/2021JG006262

Influence of Tundra Polygon Type and Climate Variability on CO_2 and CH_4 Fluxes Near Utqiagvik, Alaska

Sigrid Dengel[1], Dave Billesbach[2], and Margaret S. Torn[1,3]

[1]Earth and Environmental Sciences Area, Lawrence Berkeley National Laboratory, Berkeley, CA, USA, [2]Institute of Agriculture and Natural Resources, University of Nebraska-Lincoln, Lincoln, NE, USA, [3]Energy and Resources Group, University of California, Berkeley, CA, USA

Key Points:

- The site was a carbon sink between June and September in each of the 7 yr (2013–2019)
- Combining a polygon classification with footprint model allowed separation of fluxes by polygon type
- We recorded high methane fluxes during summer but also during freeze-up periods

Supporting Information:

Supporting Information may be found in the online version of this article.

Correspondence to:

S. Dengel,
sdengel@lbl.gov

Citation:

Dengel, S., Billesbach, D., & Torn, M. S. (2021). Influence of tundra polygon type and climate variability on CO_2 and CH_4 fluxes near Utqiagvik, Alaska. *Journal of Geophysical Research: Biogeosciences*, *126*, e2021JG006262. https://doi.org/10.1029/2021JG006262

Received 22 JAN 2021
Accepted 10 NOV 2021

Author Contributions:

Conceptualization: Sigrid Dengel
Data curation: Sigrid Dengel
Formal analysis: Sigrid Dengel
Investigation: Sigrid Dengel
Methodology: Sigrid Dengel, Dave Billesbach, Margaret S. Torn
Validation: Sigrid Dengel
Visualization: Sigrid Dengel
Writing – original draft: Sigrid Dengel, Margaret S. Torn
Writing – review & editing: Sigrid Dengel, Dave Billesbach, Margaret S. Torn

Abstract Arctic tundra has the potential to generate significant climate feedbacks, but spatial complexity makes it difficult to quantify the impacts of climate on ecosystem-atmosphere fluxes, particularly in polygonal tundra comprising wetter and drier polygon types on the scale of tens of meters. We measured CO_2, CH_4, and energy fluxes using eddy covariance for 7 yr (April to November, 2013–2019) in polygonal tundra near Utqiagvik, Alaska. This period saw the earliest snowmelt, latest snow accumulation, and hottest summer on record. To estimate fluxes by polygon type, we combined a polygon classification with a flux-footprint model. Methane fluxes were highest in the summer months but were also large during freeze-up and increased with the warming trend in August–November temperatures. While CO_2 respiration had a consistent, exponential relationship with temperature, net ecosystem exchange was more variable among years. CO_2 and CH_4 exchange (June–September) ranged between −0.83 (Standard error [*SE*] = 0.03) and −1.32 (*SE* = 0.04) μmol m^{-2} s^{-1} and 13.92 (*SE* = 0.26)—23.42 (*SE* = 0.45) nmol m^{-2} s^{-1}, respectively, and varied interannually ($p \leq 0.05$). The maximum-influence method effectively attributed fluxes to polygon types. Areas dominated by low-centered polygons had higher CO_2 fluxes except in 2016–2017. Methane fluxes were highest in low-centered polygons 2013–2015 and in flat-centered polygons in subsequent years, possibly due to increasing temperature and precipitation. Sensible and latent heat fluxes also varied significantly among polygon types. Accurate characterization of Arctic fluxes and their climate dependencies requires spatial disaggregation and long term observations.

Plain Language Summary We measured carbon dioxide and methane fluxes for 7 yr (April to November, 2013–2019) in polygonal tundra near Utqiagvik (Barrow), Alaska using eddy covariance (EC). The EC method provides the measurements of vertical flux of transported air parcels by correlation of the fluctuations in carbon dioxide or methane concentration with fluctuations in the vertical wind speed. The ice wedge polygonal tundra area is covered by ponds, drained lake basins, and wetter and drier polygon types on the scale of tens of meters across. This period saw the earliest snowmelt, latest snow accumulation date, and hottest summer on record. To estimate fluxes by polygon type, we combined a polygon classification with a flux-footprint model. The model represents the field of view of the EC system and allows the user to extract the location of the peak contribution. The site was a net carbon sink between June and September in each of the seven years. Areas dominated by low-centered polygons had higher carbon dioxide fluxes except in 2016–2017, while methane fluxes were highest in low-centered polygons 2013–2015 and in flat-centered polygons in subsequent years. This is possibly due to increasing temperature and precipitation. Not only were methane fluxes highest in the summer months but also large during freeze-up and increased with the warming trend in August–November temperatures.

1. Introduction

Among the ecosystems most vulnerable to a changing climate, Arctic tundra has relatively large stores of soil organic carbon locked within permafrost which inhibits CO_2 and CH_4 production (Hugelius et al., 2020; Schuur et al., 2009, 2015; Turetsky et al., 2020). The Arctic tundra has been a net source of atmospheric CO_2 as reported in Oechel et al. (1993, 1995) and Belshe et al. (2013) with rising temperatures accelerating permafrost thaw and subsequently CO_2 and CH_4 emissions (Keuper et al., 2020; Turetsky et al., 2020). Even with enhanced vegetation growth, the Arctic is expected to remain a net CO_2 source and become a larger CH_4 source by 2100 (de Vrese et al., 2021; Koven et al., 2015; McGuire et al., 2018; Turetsky et al., 2020). Better understanding of the timing

and magnitude of tundra responses to climate requires higher spatial-resolution observations in order to fully comprehend the effect of climate variability on carbon and energy exchange.

The Arctic coastal plain of the North Slope of Alaska is characterized by ice wedge polygonal tundra, small ponds or lakes, and drained lake basins. For example, on the Barrow Peninsula near Utqiagvik (formerly Barrow), roughly half the area is covered by low-centered polygons and lakes (24% each), with other areas covered by drier flat-centered (17%) and high-centered (11%) polygons (Lara et al., 2015; Wainwright et al., 2015). Ice wedge polygon formation is related to cycles of freezing and thawing of the active layer (Brown, 1967; Liljedahl et al., 2016), creating units that extend from a few meters to tens of meters across. The different polygon types differ in soil microbial community (Graham et al., 2013; Jansson et al., 2012; Taş et al., 2018), soil organic carbon content (Bockheim et al., 1999; Dennis et al., 1978; Michaelson et al., 1996), hydrology and inundated area (Brown, 1967; Liljedahl et al., 2016; Zona et al., 2011), and vegetation cover (Dennis et al., 1978; Webber, 1978). These diverse properties of tundra landscape combine to spatially diverging CO_2 and CH_4 fluxes across the landscape as shown in many high latitude studies (e.g., Pirk et al., 2017 and references therein).

The Arctic is undergoing a warming trend (Box et al., 2019; Jeong et al., 2018; Moritz et al., 2002) causing later active-layer freeze-up (Box et al., 2019) as well as a deepening of the active layer (Andresen et al., 2020; Gewirtzman et al., 2018). Along the Arctic coastal plain of Alaska, active layer depth (ALD) varies at fine scale due to microtopography, vegetation, snow dynamics, and belowground properties, such as soil moisture for example, but a trend of deepening ALD has been observed at some locations. For example, at the Barrow Environmental Observatory, near Utqiagvik and environs where this study was based, ALD deepened between 2000 and 2015 as found by the recent modeling study by Yi et al. (2018), integrating remote sensing and field observations. This said, a declining trend (ALD shallower) was observed from manual annual probing at the site between 1995 and 2007 by Streletskiy et al. (2008), coinciding with a period of global warming hiatus (Dai & Wang, 2018) with an average maximum depth of 0.39 m ($SE = 0.01$) in 2013–2018 (D. Nicolsky, University of Alaska, Fairbanks [personal communication]; Romanovsky et al., 2017) usually reached in mid to end August (Shiklomanov et al., 2010; Streletskiy et al., 2008). Precipitation may also be trending, with recent studies showing an increase across Alaska (Wendler et al., 2017) and the greater pan-Arctic region (Box et al., 2019). In Utqiagvik, winter and spring precipitation are increasing (McAfee et al., 2013). Models project that climate changes such as these will alter the functioning and composition of polygonal tundra (Lara et al., 2018), including altering greenhouse gas and energy fluxes (Grant et al., 2019; Grant, Mekonnen, Riley, Wainwright, et al., 2017; Jeong et al., 2018; López-Blanco et al., 2017).

While net CO_2, CH_4, and energy exchange at the landscape scale are measured in the Arctic using the well-established eddy covariance (EC) technique (Aubinet et al., 2012; Baldocchi, 2003), partitioning Arctic CO_2 fluxes into ecosystem respiration and gross primary productivity (GPP) is less straightforward than in many other locations due to the lack of true night during the growing season.

One approach to measuring fluxes from small landscape features is the chamber method (Kutzbach et al., 2007; Norman et al., 1997; Pavelka et al., 2018). Chamber measurements of greenhouse gas fluxes in polygonal tundra show high variability in relative CO_2 flux rates among polygon types and saturation. For example, some studies report lower ecosystem respiration in low-centered polygons when the ground was wetter (Olivas et al., 2011) in comparison to drier periods (study only looked at low-centered polygons) while Pirk et al. (2017) measured higher respiration in wetter areas (no polygon type indicated) at their polygonal tundra site. Wilkman et al. (2018) reported consistently higher respiration rates in troughs and low centered polygons in comparison to high-centered polygons. However, Vaughn et al. (2016) found no significant difference among polygon types. These results illustrate the high variability in respiration in this spatially and temporally heterogeneous environment. In contrast, methane chamber measurements in tundra ecosystems appear more predictable, with consistently higher efflux in low-centered polygons and troughs, and efflux in flat-centered polygons only during wetter periods (Lara et al., 2015; Sachs et al., 2010; Vaughn et al., 2016; von Fischer et al., 2010; Wagner et al., 2003). While chamber measurements are useful for characterizing controls of fluxes by plant, moisture, and temperature conditions, their fine scale (<1 m^2) and intermittent deployment—continuous chamber measurements especially tend to be poorly replicated—makes scaling up over space and time challenging. In contrast, the EC method captures the turbulent exchange continuously and over a larger area up to 1 km^2 depending on atmospheric stability (Burba, 2001). The incommensurate nature of these measurements complicates scaling chamber fluxes to the

ecosystem level or using flux data to provide mechanistic explanations for observed EC fluxes (Fox et al., 2008; Zhang et al., 2012). Additional means of attributing EC fluxes to landscape features are needed.

Footprint studies (Kljun et al., 2004; Kormann & Meixner, 2001) help in estimating the field of view of EC measurements at larger scale, but have not been applied to quantify fluxes from smaller or distinct landscape features, such as different polygon types. The polygon classification work by Wainwright et al. (2015) opens up a new measurement avenue in which polygon distribution, footprint analysis, and the maximum-effect source location within the footprint (estimated for each half-hourly flux value) and its distance from the EC tower can be combined to attribute flux components to locations within the footprint or to specific landscape types.

Although EC measurements cover a spatially small area (footprint) of up to a few hundred meters with sites across the Arctic still limited in numbers, their data are nonetheless used in estimating regional fluxes of CO_2 (Ueyama et al., 2013), CH_4 (Sayres et al., 2017; Zona et al., 2016), or energy fluxes (Cristóbal et al., 2017). The spatial heterogeneity of the Arctic polygon tundra has large implications for regional fluxes and land surface models and the fidelity and uncertainty of their predictions. A synthesis of 40 terrestrial models' simulations of Alaska (Fisher et al., 2014) showed almost no consistent spatial patterns in net ecosystem exchange (NEE). Different models showed the entire state as a strong carbon sink, while others showed the opposite. Some predicted carbon neutral emissions and some models showed a spatial distribution of sinks and sources, as also did a newer study by Commane et al. (2017).

A model study on energy fluxes of the North Slope of Alaska (Lynch, Bonan, et al., 1999; Lynch, Chapin, et al., 1999) detailed the difficulty of model validation and performance using measured data from multiple meteorological and/or EC sites and research groups, highlighting the uncertainties attached to measurement methods, instruments, and model parametrization. Uncertainties that accompany such measurements vary from EC tower/met station location to the exact placement and depth of the individual soil temperature probe or soil heat-flux plates and their respective spatial representativeness. These observational challenges and model studies highlight the difficulties in understanding and predicting the complex and heterogeneous Arctic polygon tundra, and its dynamics under a changing climate.

To better understand the temporal and spatial heterogeneity of CO_2, CH_4, and energy exchange at the Next Generation Ecosystem Experiments (NGEE Arctic) Barrow research site near Utqiagvik, Alaska, we analyzed seven consecutive years of EC and meteorological measurements covering April to November, 2013–2019. This period represents some meteorological extremes, including the earliest snowmelt dates, latest snow accumulation dates (Cox et al., 2017), and hottest summer on record (National Oceanic and Atmospheric Administration [NOAA], 2019). The objectives of this study were to (a) document the inter- and intra-seasonal variation in CO_2, CH_4, and energy fluxes at a polygonal tundra site; (b) explore how variability and trends in meteorological variables affect these fluxes; and (c) investigate the spatial variability of these fluxes, to ultimately (d) assess the possibility of separating these landscape-scale fluxes by polygon type.

2. Materials and Methods

2.1. Site Description

This study was carried out in the Barrow Environmental Observatory (BEO, 71°16′48.26″N; 156°36′33.12″W) on the coastal plain near Utqiagvik (Barrow), Alaska, as part of the United States Department of Energy Next Generation Ecosystem Experiments (NGEE-Arctic) project (Figure 1). The mean annual temperature is −12°C and mean annual precipitation is 114.3 mm. The site is characterized by polygonal structures classified into low-, flat-, and high-centered polygons, each representing a different microtopography and hence surface, soil, and hydrological properties (Brown, 1967; Liljedahl et al., 2016; Wainwright et al., 2015; Zona et al., 2011). These features are identifiable in aerial images (Cherry & Crowder, 2016; Svensson, 1963) and in high-resolution elevation models (Wilson & Altmann, 2017). According to Lara et al. (2015) and Wainwright et al. (2015), low-centered polygons occupy the largest area across the Barrow Peninsula and the BEO, followed by flat-centered ones, and high-centered polygons only cover around 11% of the tundra. Areas north of the EC tower site (AmeriFlux ID US-NGB, Figures 1 and 2) are dominated by low-centered polygons while the southern and western sections by flat- and high-centered polygons. The main vegetation types found across the BEO are Carex aquatilis subsp. Stans, Saxifraga cernua communities, Luzula confusa, Dupontia fisheri as well as non-acidic tundra Carex spp. and Eriophorum spp. (Sloan & Norby, 2014; Villarreal et al., 2012).

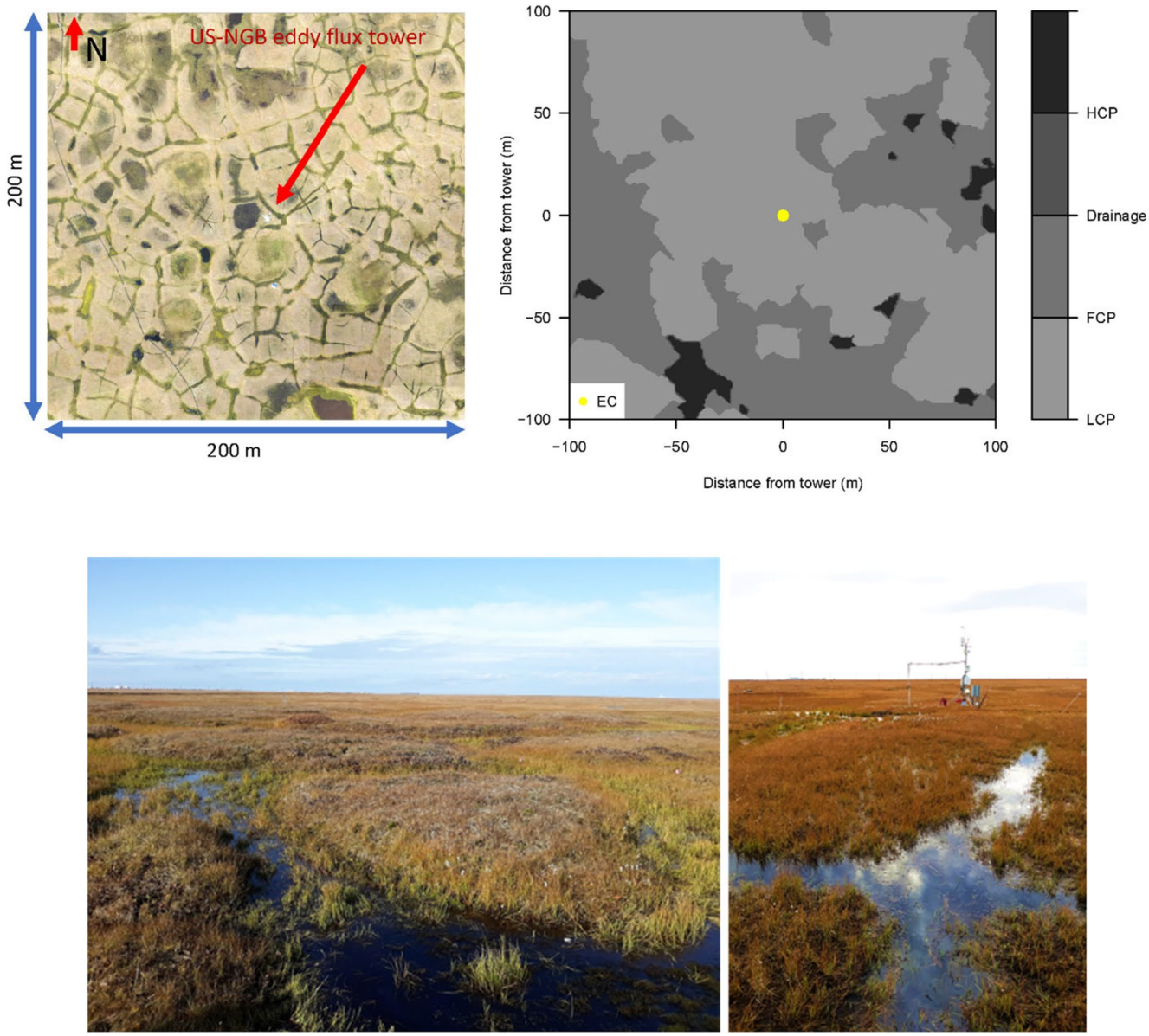

Figure 1. Aerial image (upper left image) of the area surrounding the eddy flux tower together with the polygon classification extracted from Wainwright et al. (2015; upper right image) in which the location of the EC tower is marked as a yellow dot. The lower panel shows images of polygonal features near the NGEE Arctic Barrow eddy flux site (early September 2019) showing an area dominated by flat and high centered polygons surrounded by inundated troughs. Photo credit: J. Cherry, NGEE Arctic (aerial image) and S. Dengel (lower panel images).

2.2. Methods

2.2.1. EC Measurements

We measured CO_2, CH_4 and energy exchange at the landscape level at the NGEE-Arctic eddy flux site (Dengel et al., 2020; Torn & Dengel, 2020) using EC for 7 yr (April to November, 2013–2019) with a 74% overall April–November data coverage (30 min data) and 79% for the June–September data range. The system consisted of a Gill R3-50 ultrasonic anemometer (Gill Instruments, Lymington, UK), and an open path LI-7500A CO_2/H_2O gas analyzer (LI-COR Biosciences, Lincoln, NE, USA), along with an LI-7700 CH_4 gas analyzer (LI-COR Biosciences) at 4 m above ground. Digital raw data streams from all three of these instruments were synchronized and recorded by a program (HuskerFlux) developed by D. Billesbach; running on a small, single-board computer, which also provided communications for data retrieval, and served as a platform for the Campbell

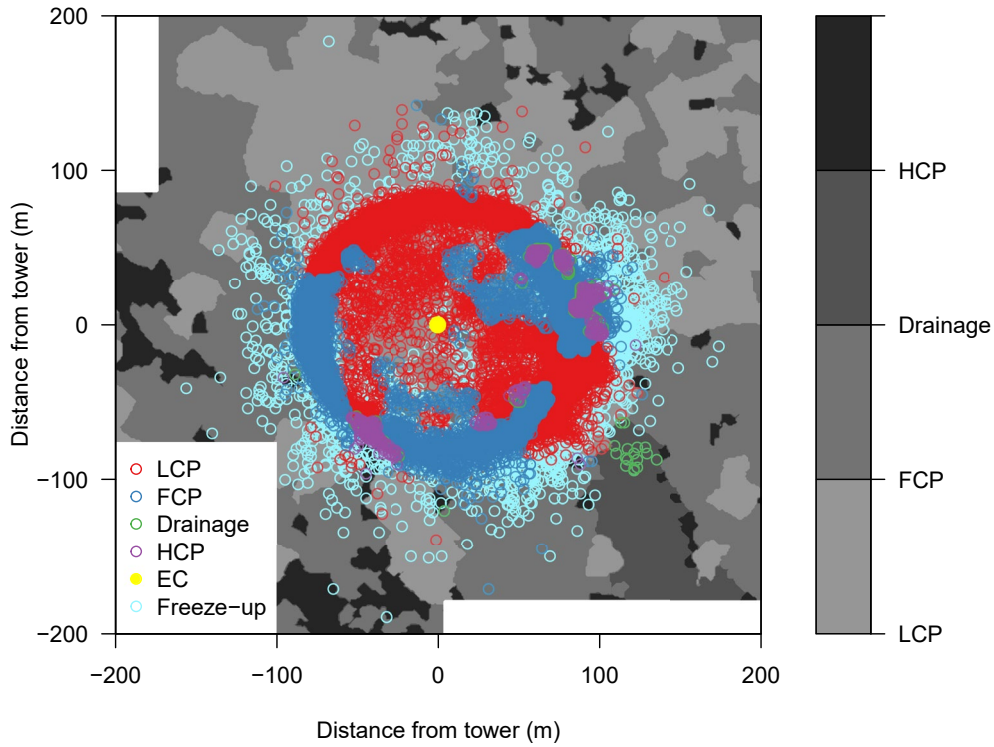

Figure 2. Maximum flux-contribution locations for fluxes color-coded by polygon type. The location of each individual (each half-hour value) estimated maximum flux-contribution location is overlaid on a polygon map, showing low-centered (LCP), flat-centered (FCP), high-centered (HCP) polygons and the drainage area (drainage, to the southeast of the eddy flux tower) in gray tones. The solid yellow circle in the center of the figure shows the location of the eddy flux tower, while the cyan-colored circles show measurements outside the June–September period (freeze-up) and with them the seasonal shift in footprint extent as those maximum flux-contribution locations are further away than those estimated for June to Septemeber.

Scientific LoggerNet program which archived raw data from other (slow response) instruments. The following processing steps were taken in calculating 30-min fluxes from the raw 10 Hz data: spike detection was implemented using the standard Vickers and Mahrt (1997) de-spiking algorithm. We applied the coordinate rotation using the second rotation method described in Baldocchi et al. (1988), sonic virtual temperature correction (Kaimal & Gaynor, 1991), frequency response correction (Massman, 2000), and the buoyancy flux correction defined in Schotanus et al. (1983). The computed co-spectra for vertical wind and temperature, CO_2, CH_4, and H_2O, respectively, for each half hour using the Fast Fourier Transform were used to verify the magnitude of the frequency response correction, reflecting the ability of the system to measure high-frequency gas transport. We applied the Webb-Pearman-Leuning density correction (WPL; Webb et al., 1980) to the data originating from both gas analyzers, as well as the LI-7700-specific corrections for spectroscopic effects (LI-COR, 2010; McDermitt et al., 2011). Furthermore, data quality control measures were carried out following guidelines given in Foken et al. (2004) by removing flux values with quality flags of seven and higher, in addition to excluding flux data recorded under low signal strength and rainy periods as rain has an impact on the performance of open-path gas analyzers as well as sonic anemometers (Burba, 2013). These quality control procedures, together with fluxes filtered for low friction velocity led to a removal of 38% of measured CO_2 fluxes (27% for June–September time periods). In addition to the friction-velocity filter, one of the common reasons for data removal was low signal strength.

Due to its proximity to the Chukchi Sea, the site experiences prolonged periods when the foggy air is enriched with salty sea air leading to low signal strength values, sometimes within hours of cleaning the optical windows of the open path analyzers. Furthermore, the site experiences extensive periods without power.

2.2.2. Meteorological Measurements

Meteorological measurements were made along with the EC measurements (April to November, 2013–2019). The suite of instrumentation included air temperature and relative humidity (HMP60, Campbell Scientific, Logan, UT, USA) measured at 3 m above ground (overall data coverage 80%, 93% for June–September time periods, and similar coverage for all other met variables), incoming and outgoing short- and longwave radiation (CNR4, Kipp & Zonen, Delft, The Netherlands), and incoming and reflected photosynthetic photon flux density (PPFD) that was measured with two LI-190 quantum sensors (LI-COR Biosciences) at 2 m above ground. Surface temperature was measured using a SI-111 Infrared Radiometer (Apogee Instruments, Logan, UT, USA) with a 22° half-angle field of view attached at 2 m above the ground. These IR sensors use a portion of the longwave thermal radiation emitted by the surface (i.e., tundra) within the field of view. Soil heat flux (G) was measured with four soil heat flux plates (Hukseflux, Delft, The Netherlands) at 7 cm below the surface in the vicinity of the EC tower. No attempt was made to estimate the heat flux above the soil heat flux plates or at surface level. These meteorological data (Dengel et al., 2020) were quality controlled following methods briefly introduced in Christianson et al. (2017) and Pastorello et al. (2017) by removing observations outside realistic margins, as well as correcting for timestamp drifts, instrument drift, or use of wrong coefficients, for example, soil temperatures at 10 cm depth were measured at five locations along a transect across polygons near the EC tower by Romanovsky et al. (2017). Daily thaw depth values were estimated from soil temperature readings recorded along a vertical profile in the center of a polygon to a depth of 1.5 m (Romanovsky et al., 2017).

2.2.3. Flux Partitioning, Gap Filling, Calculation of Cumulative Fluxes, and Energy Balance

Due to the late snowmelt season (mostly June) and early autumn snow accumulation that is often already occurring in September (Figure 3, see incoming and reflected radiation) only June–September data were partitioned into ecosystem respiration and GPP. To do so ecosystem respiration was calculated from relationships between nocturnal NEE and soil temperature measured within the footprint area. Windy (friction velocity > 0.15 m s^{-1}) nighttime flux data (PPFD < 50 µmol m^{-2} s^{-1}, as also used by Euskirchen et al., 2012; Nordstroem et al., 2001 at their Arctic sites) were plotted against soil temperature and an exponential function (Lloyd & Taylor, 1994) fitted. Currently there is no consent on use of soil versus air temperature in Arctic ecosystem respiration studies (Euskirchen et al., 2012, 2014, 2017; Grøndahl & Ministry of the Environment-Denmark, 2006; Kutzbach, 2006; Shaver et al., 2013; Vourlitis et al., 2000; Zamolodchikov et al., 2003) with air temperature generally being used due to its more frequent availability, as stated by Keenan et al. (2019). Ecosystem respiration represents the sum of heterotrophic (soil) respiration that is driven by soil temperature and moisture, and autotrophic respiration that is driven by air temperature (Ruimy et al., 1995) so a combination of both appears most appropriate. Wohlfahrt and Galvagno (2017) pointed out that the use of soil temperature as the driving temperature underestimates daytime respiration while the use of air temperature as the driving temperature to overestimate daytime respiration. In order to obviate such an under- or overestimation of daytime respiration we plotted nighttime fluxes against soil temperature and used air temperature to estimate daytime respiration and GPP. We believe this to be the appropriate method at this site as this method avoids this bias together with the additional uncertainty introduced by thermal inertia/thermal offset and the resulting time lag of Arctic soil temperature in relation to air temperature (Aalto et al., 2018; Biskaborn et al., 2019; Lyu, 2015; Lyu & Zhuang, 2018; Zhang et al., 2005) and its effect on respiration (Shaver et al., 2013).

Following Causton and Dale (1990) and Ruimy et al. (1995), the Michaelis-Menten rectangular hyperbola was used to describe the relationship between photosynthesis (GPP) and PPFD, representing the apparent photochemical efficiency (light use curve):

$$F = \frac{A_{max} Q_g}{\left(b + Q_g\right)},$$

where Q_g is the incident PPFD, A_{max} the maximum gross photosynthesis at infinite irradiance, and b is the PPFD value at which half of the light-saturated photosynthesis is occurring. A_{max}/b is the slope of the curve at $A_{max} = 0$, representing the apparent photochemical efficiency (light use efficiency [LUE]; Causton & Dale, 1990).

In order to calculate the net carbon (g C m^{-2}) cumulative uptake of the site, gap-free data are required. Following the same procedure as with partitioning NEE, we only gap-filled NEE for June–September by applying the AmeriFlux ONEFlux Marginal Distribution Sampling (Pastorello et al., 2020) gap-filling procedure incorporating

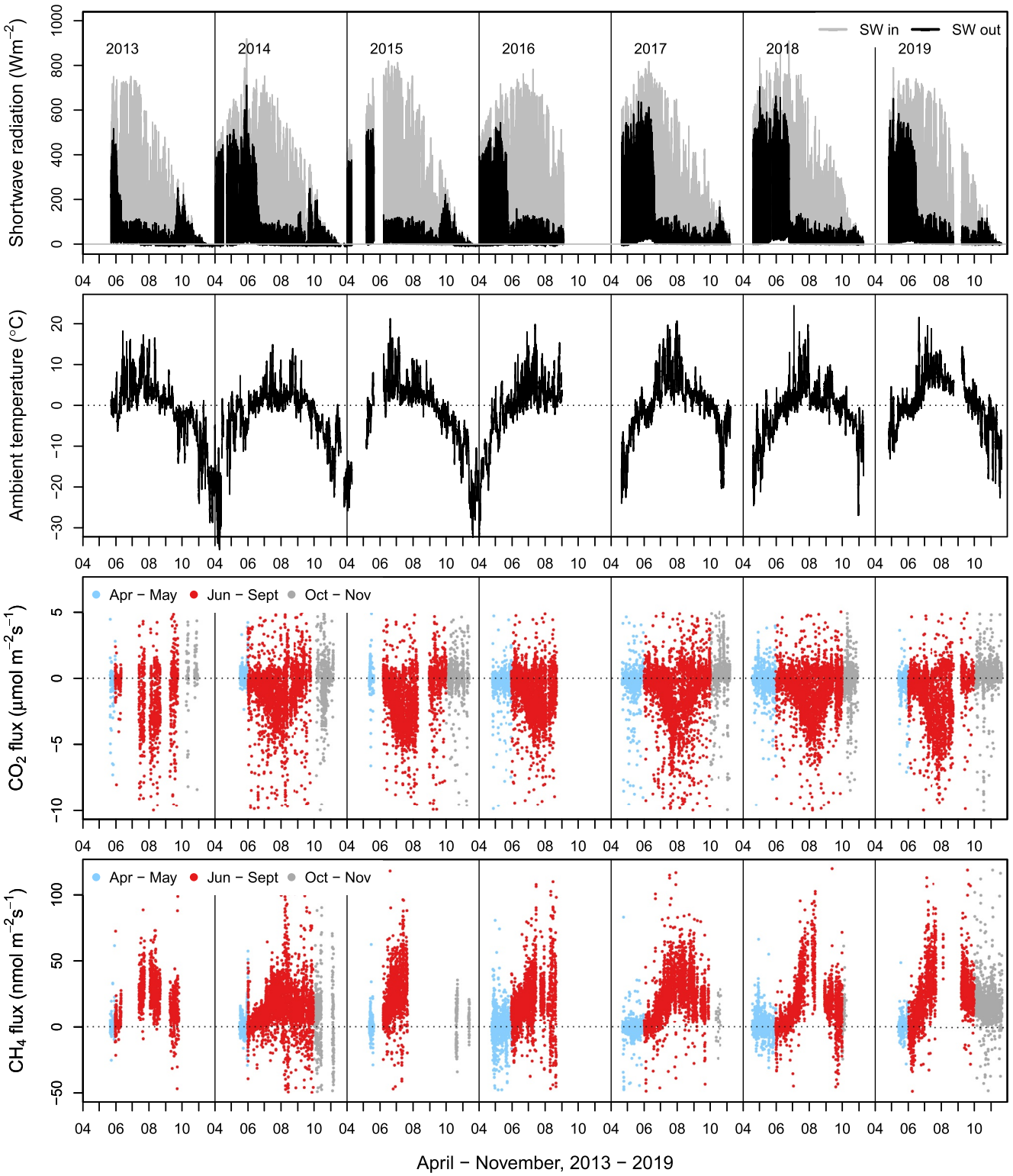

Figure 3. Overview of meteorological and flux data measured at the Barrow Ecological Observatory near Utqiaġvik (formerly Barrow), Alaska, showing incoming (in gray) and outgoing (in black) shortwave radiation in the upper most panel, air temperature (in black), and CO_2 and CH_4 fluxes color coded by spring (April–May, in light blue), June–September (in red), and freeze-up season (October–November in gray). Vertical lines are added to distinguish between individual years and horizontal lines at $y = 0$ added for clarity only (gray in upper most figure and dotted black in the subsequent three lower figures). Numbers under the x-axis represent months.

Table 1
Monthly and June–September Averages for Air Temperature (TA—°C), CO_2 Fluxes (FC—μmol m^{-2} s^{-1}), CH_4 Fluxes (FCH_4—nmol m^{-2} s^{-1}), Latent Heat (LE—W m^{-2}) and Sensible Heat (H—W m^{-2}), Together With Monthly and June–Septemeber Total Precipitation (Prec—mm) and the June–September Averaged Gap-Filled (FC_{gf}) CO_2 Fluxes

Month ave.	2013				Mean ± *SE*	2014				Mean ± *SE*
Variance (mean and *n*)	June	July	August	September	June–September	June	July	August	Sepembert	June–September
TA	2.92 (1,391)	5.58 (1,415)	2.99 (1,421	−1.21 (1,438)	2.56	0.55 (1,440)	2.78 (1,486	2.95 (1,391)	0.68 (1,377)	1.75
Prec	16.3	34.8	33.1	32.8	117	37.2	23.9	18.3	33.8	113.2
FC	−0.19 (202)	−1.99 (207)	−2.05 (417)	−0.61 (322)	−1.31 ± 0.07	−0.59 (774)	−1.37 (948)	−1.23 (657)	0.13 (521)	−0.86 ± 0.04
FCH4	5.70 (213)	29.39 (226)	28.18 (439)	12.57 (428)	19.61 ± 0.42	4.72 (989)	18.53 (1,064)	19.10 (873)	13.54 (896)	13.92 ± 0.26
LE	31.86 (232)	39.05 (283)	31.81 (557)	15.09 (461)	28.13 ± 0.78	32.23 (1,187)	41.18 (1,213)	26.70 (901)	17.60 (736)	31.02 ± 0.51
H	34.17 (248)	47.64 (326)	36.35 (663)	11.16 (586)	29.97 ± 0.97	40.62 (1,342)	64.72 (1,401)	44.53 (1,223)	6.12 (1,182)	40.19 ± 0.78
FC_{gf}					−0.89 ± 0.02					−0.45 ± 0.02

Monthly average	2017				Mean ± *SE*			2018
Variance (mean and *n*)	June	July	Aug	September	June–September	June	July	August
TA	0.76 (1,433)	7.41 (1,483)	4.18 (1,484)	1.68 (1,436)	3.54	−0.03 (1,438)	5.74 (1,482)	1.90 (1,484)
Prec	8.4	36.4	47.9	20.3	113	8.2	39	29.3
FC	−0.19 (982)	−1.86 (926)	−1.40 (760)	−0.16 (576)	−0.95 ± 0.04	−0.18 (729)	−1.16 (890)	−1.60 (869)
FCH4	4.69 (1,013)	26.98 (796)	34.49 (763)	17.55 (392)	20.05 ± 0.33	3.31 (1,025)	26.17 (601)	41.70 (194)
LE	25.85 (1,192)	37.39 (1,197)	25.13 (1,003)	15.47 (816)	26.95 ± 0.47	14.1 (1,164)	42.35 (1,157)	22.36 (1,152)
H	31.33 (1,236)	40.86 (1,285)	15.33 (1,345)	5.04 (1,140)	23.49 ± 0.54	15.64 (1,155)	43.41 (1,395)	24.62 (1,337)
FC_{gf}					−0.73 ± 0.02			

Note. In addition, number of datapoints for each month are added in brackets as well as the standard error of the means (*SE*), as a measure of uncertainty, are included for all fluxes (June–September averages).

incoming shortwave radiation, air temperature, and vapor pressure deficit which act as drivers of net fluxes. Missing meteorological values have implications for gap-filling methods/procedures and associated uncertainties (see Reichstein et al., 2005). The site had no power in September 2016 and to avoid introducing very high uncertainties no attempt was made to gap-fill missing September 2016 values and so this month was not included in the cumulative sums. Gap-filled averages and associated standard errors for each June–September (2013–2019) period are reported in Table 1. A detailed description of the method, procedures, and uncertainties can be found in Reichstein et al. (2005; Appendix A) and Pastorello et al. (2020). CH_4 flux data were not gap-filled.

Energy balance was calculated as the fraction of the total sum of latent, sensible and soil heat flux, and the net incoming and outgoing radiation measured at the site. While latent and sensible heat were measured with the EC suite of instrumentation, net radiation was measured off the EC tower and ground heat flux plates installed near the tower. This common measurement method is well known to be accompanied with uncertainty introduced by the combination of a varying footprint (potentially each half hour) and fixed point measurements.

2.2.4. Polygon Classification and Footprint Determination: Maximum Influence Estimation

Since source and sink locations are dependent on the underlying surface, in our case polygonal features, we include the polygon type classification introduced in Wainwright et al. (2015) in conjunction with a simple application of the Kljun et al. (2004) Lagrangian footprint model.

The ability of this model to predict the area of influence (footprint/field of view of the EC system) and the maximum-effect source location (location with the highest contribution) within the footprint (estimated for each half-hourly flux value) and its distance from the EC tower are key to our analysis. The spatial extent of an individual footprint and distance to the maximum contribution location depends on measurement height, surface roughness, atmospheric stability, wind direction, and friction velocity. Due to the fine-scale heterogeneity of the site no attempt was made in classifying each individual footprint in the current study.

2015				Mean ± *SE*	2016				Mean ± *SE*
June	July	August	September	June–September	June	July	August	September	June–September
6.19 (1,132)	4.33 (1,486)	3.35 (1,488)	−0.60 (1,439)	3.17	2.07 (1,438)	5.20 (1,484)	3.04 (1,356)	3.08 (26)	3.46
20	6.7	40.6	18.5	85.8	18	28.9	17.4	19.9	84.2
−1.01 (748)	−2.46 (908)	−1.82 (259)	−0.02 (714)	−1.32 ± 0.04	−0.42 (1,110)	−1.71 (1,023)	−1.09 (439)		−1.04 ± 0.03
20.59 (899)	31.04 (673)			25.06 ± 0.45	12.76 (1,238)	25.47 (808)	21.29 (336)		18.27 ± 0.35
56.53 (981)	38.51 (1,258)	33.17 (362)	15.60 (1,016)	36.43 ± 0.62	45.00 (1,297)	39.69 (1,256)	21.30 (712)		37.79 ± 0.61
58.33 (1,063)	61.11 (1,345)	32.85 (422)	7.86 (1,274)	40.95 ± 0.85	62.16 (1,375)	60.92 (1,407)	34.47 (843)		55.24 ± 0.97
				−0.84 ± 0.02					−0.74 ± 0.02

	Mean ± *SE*	2019				Mean ± *SE*
September	June–September	June	July	August	September	June–September
3.01 (414)	2.24	1.99 (1,440)	8.44 (1,488)	5.60 (1,111)	3.67 (1,121)	4.99
11.8	88.3	21.1	67.5	65.2	22.9	176.7
−0.37 (645)	−0.83 ± 0.03	−0.50 (868)	−2.40 (834)	−1.66 (605)	0.04 (380)	−1.27 ± 0.04
13.7 (680)	14.61 ± 0.36	7.60 (855)	40.25 (566)	55.76 (10)	28.73 (690)	23.42 ± 0.45
10.96 (846)	23.26 ± 0.44	32.13 (1,138)	37.95 (1,086)	27.63 (723)	14.1 (573)	30.07 ± 0.55
8.79 (1,048)	23.12 ± 0.56	36.91 (1,289)	35.07 (1,374)	17.90 (969)	1.17 (990)	24.3 ± 0.59
	−0.52 ± 0.02					−0.74 ± 0.02

Furthermore, footprint models assume stationarity of the flux across space and time. In order to combine these spatial and surface characteristics we overlaid the polygon type (LCP, FCP, and HCP) across coordinates on a map, allocating coordinates to each maximum flux contribution location derived from wind direction and distance allowing an attribution of fluxes to polygon type (Figure 2) while acknowledging the potential uncertainty introduced due to the conversion of microtopography to a plane surface, a common feature at complex sites.

2.2.5. Statistics

We applied the bootstrapping approach (Banjanovic & Osborne, 2016) by resampling the flux data 10,000 times (with replacement) in order to compare the true/population means by looking at their confidence intervals together with the difference in means across all June–September periods as well as by polygon type and the degree of significance of differences between individual comparison pairs. The Mann-Kendall (Kendall, 1975; Mann, 1945) and the modified Mann-Kendall trend analysis (Hamed & Rao, 1998) commonly applied in hydrometeorological time series (Wang et al., 2020 and reference therein) but also EC time series (Euskirchen et al., 2017) was applied to the data in order to investigate existing trends in fluxes or meteorological conditions over time and the statistical significance thereof. Prior to applying the modified Mann-Kendall trend analysis we assessed the data for existing autocorrelation and partial autocorrelation, a procedure common in time series analysis, as autocorrelation is known to increase the chances of detecting significant trends where in fact there are none. Results summarize the Kendall rank correlation coefficient (τ) indicating the trend strength ($-1 < \tau < 1$) as well as the magnitude (S) of the trend (Sen's slope [Sen, 1968], change in flux) together with the significance at the 95% level ($p \leq 0.05$) of the observed trend. These analyses were applied to daily averages treated separately by the three time periods: snowmelt (April and May), June–Septemeber, and freeze-up (October and November) as well as separated by polygon type.

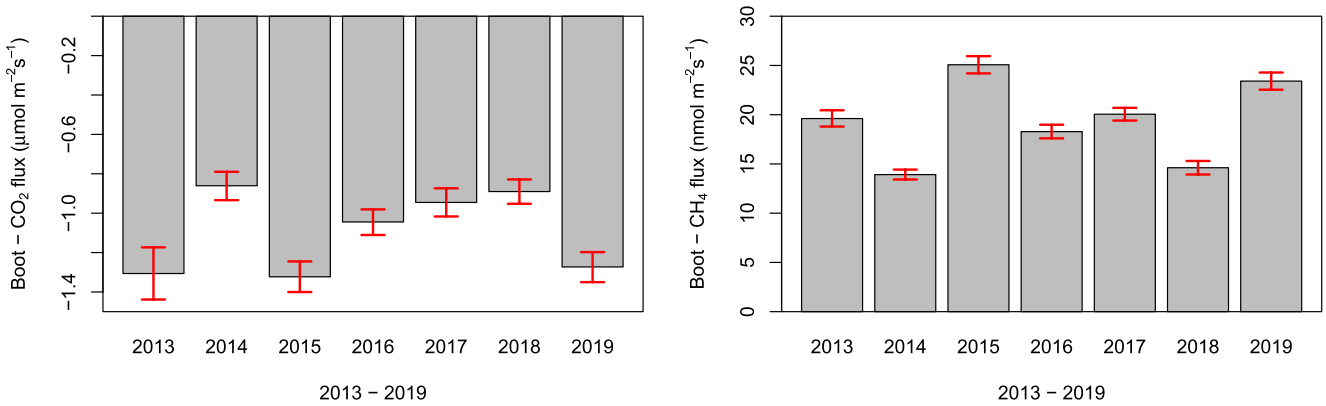

Figure 4. Mean CO_2 and CH_4 fluxes, together with their respective confidence intervals (CI) at 95% level (including the 2.5th and 97.5th percentile of the bootstrap distribution) after applying bootstrapping (10,000 resamples with replacement) to the data.

3. Results

3.1. Temporal Variability in Net CO_2 Exchange, GPP, and Respiration Over 7 yr

NEE averaged over April to November (Table S1) ranged from −0.59 ($SE = 0.03$) µmol m^{-2} s^{-1} in 2017 to −1.06 ($SE = 0.06$) µmol m^{-2} s^{-1} in 2013 (negative values indicate carbon uptake from the atmosphere) and NEE averaged over June–September varied from −0.83 ($SE = 0.03$) µmol m^{-2} s^{-1} in 2018 to −1.32 ($SE = 0.04$) µmol m^{-2} s^{-1} in 2015 (Figure 3 and Table 1). There were significant differences in fluxes between some years (bootstrapped, 95% confidence level using the percentile method; Figure 4), that are partially explained by variation in climate over these seven years (see Section 3.4). For example, we can say with 95% confidence that 2013 fluxes were somewhere between −0.30 up to −0.60 µmol m^{-2} s^{-1} higher (sign convention, more uptake) than 2014, but 2013 was not different from 2015, having been 0.17 µmol m^{-2} s^{-1} lower than 2015 up to −0.14 µmol m^{-2} s^{-1} higher than 2015 (see confidence interval values in Table S2 for all CO_2 [by year] comparisons).

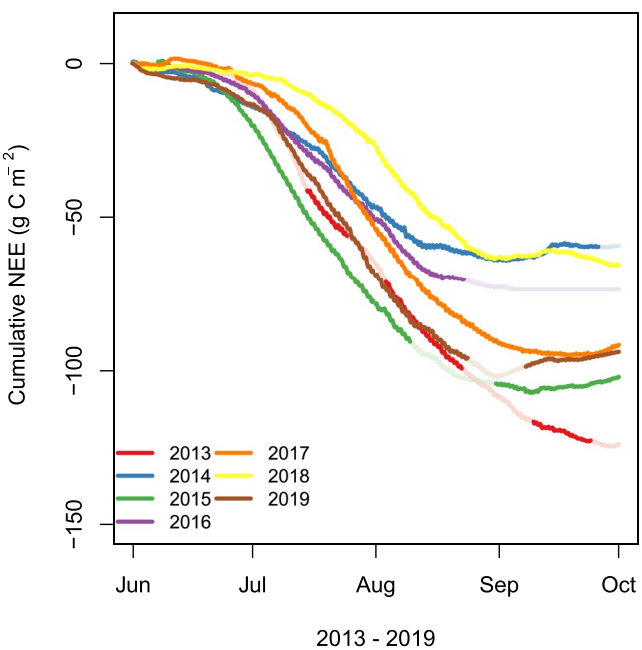

Figure 5. Cumulative net CO_2 flux (NEE) for June toSeptember, 2013–2019 estimated from gap-filled data. Gaps longer than 5 days are highlighted in pale colors. Due to loss of power at the site there are no data available for September 2016 and simply visualized as a straight pale colored line.

The tundra was a net sink of CO_2 in each of the June–September periods (Figure 5) with 65.4–102.1 g C m^{-2} cumulative net uptake. Late summer/early autumn uptake seen in Figure 5 can possibly be explained by warm temperature spells promoting continuation in biomass growth and carbon uptake (see September averages for air temperature and CO_2 fluxes in Table 1). No clear trend with length of the snow-free season was found.

There was a weak but significant decreasing trend in April–November NEE over the 7 yr (becoming more positive) with $\tau = +0.066$, $p = 0.080$ with an average daily change rate of $S = 0.0003$ µmol m^{-2} s^{-1} but not for the June–September values.

The weak decreasing trends for April and May (snowmelt) and Octoberand November (freeze-up/post photosynthetic season) periods were not significant (Table S3).

GPP, based on partitioning NEE, was highest in 2013 and lowest in 2014. To investigate ecosystem efficiency in converting light into photosynthate, we estimated the LUE as the relationship between PPFD and GPP. The response is asymptotic (fitted rectangular hyperbola, Figure 6), with parameters depending on leaf photosynthetic properties and the environment: In our case it describes gross photosynthesis, and so the curve passes through the origin. Parameters estimated from the Michaelis-Menten rectangular hyperbola (A_{max}, b, and LUE) for each month separately are summarized in Table S4. June–September GPP and LUE by polygon type were not significantly different from each other.

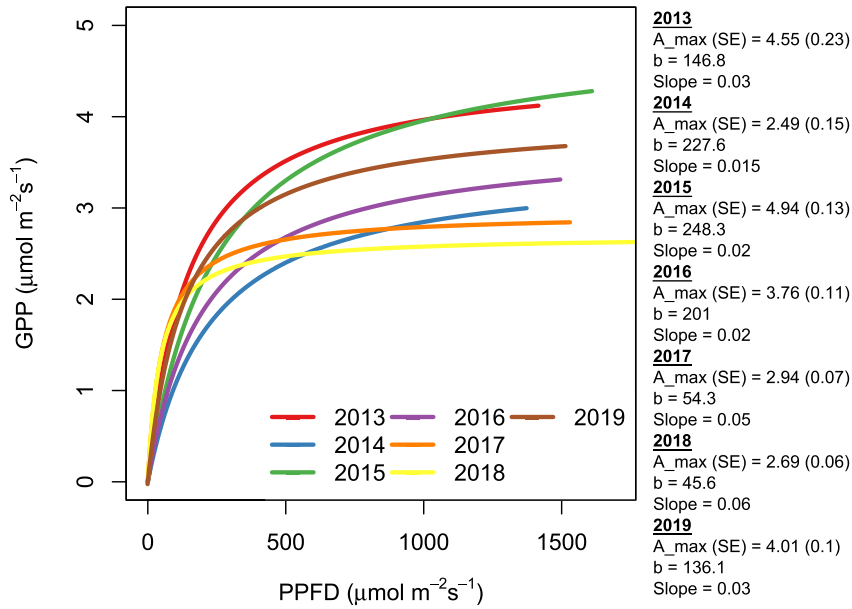

Figure 6. Estimated light use efficiency (LUE) curves as the relationship between photosynthetic photon flux density and gross primary productivity for June to September, 2013–2019, together with the respective parameters indicating the LUE of the polygon tundra for each June–September period. The estimated goodness of fit (R^2) for the individual fitted rectangular hyperbola of 0.27, 0.22, 0.40, 0.28, 0.15, 0.18, and 0.26 for 2013–2019, respectively, should be taken with caution since R^2 values for non-linear regressions are not always representative.

June–September average ecosystem respiration was lowest in 2014 and highest in 2019. High resolution (half hourly) values increased exponentially with increasing surface temperature (Figure 7).

No relationship with amount of precipitation nor a lag between respiration and precipitation was found. As with NEE, no significant trend was observed in GPP nor respiration over the seven June–September periods.

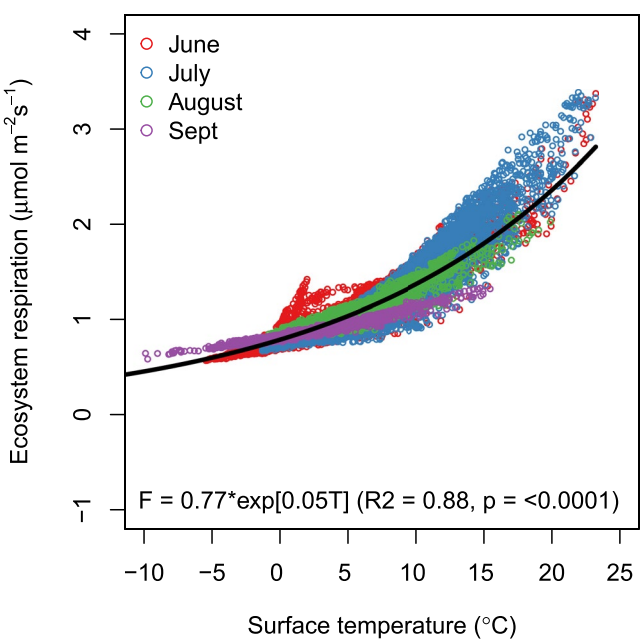

Figure 7. Ecosystem respiration as a function of surface temperature for June to September, 2013–2019 color coded by months.

3.2. Methane Fluxes

CH_4 fluxes averaged over each April to November (Table S1), 2013–2019 period ranged between 10.05 (SE = 0.25) nmol m^{-2} s^{-1} in 2018 to 19.83 (SE = 0.41) nmol m^{-2} s^{-1} in 2015, while June–September (Table 1) averages ranged from 13.92 (SE = 0.26) nmol m^{-2} s^{-1} in 2014 to 23.42 (SE = 0.45) nmol m^{-2} s^{-1} in 2019 (Table 1). Averaged over all years, June–September CH_4 flux was 18.44 (SE = 0.14) nmol m^{-2} s^{-1}. Figure 8 shows the cold-season (April and May/spring snowmelt and October and November/fall freeze-up) distribution of CH_4 fluxes outside the typically reported snow-free June–September period as well as the whole April–November data range.

According to Mann-Kendall analysis, there appears to have been an increasing trend in June–September methane fluxes over these seven years (Mann-Kendall analysis, τ = +0.111, p = 0.01) with an average change rate of 5.47 nmol m^{-2} s^{-1} per year. Spring (April andMay) fluxes were very low, averaging 1.1 (SE = 0.1) nmol m^{-2} s^{-1} with no significant trend across years. In contrast, fall (October and November) CH_4 fluxes, which averaged 13.93 (SE = 0.34) nmol m^{-2} s^{-1}, had a significant increasing trend with an average change in rate of 0.125 nmol m^{-2} s^{-1} day^{-1} (p = 0.029; Table S2).

As with CO_2 fluxes, the June–September CH_4 flux averages varied significantly between some but not all years (Figure 4). Methane fluxes in 2013 were higher than 2014, somewhere between 4.75 and 6.68 nmol m^{-2} s^{-1} (95%

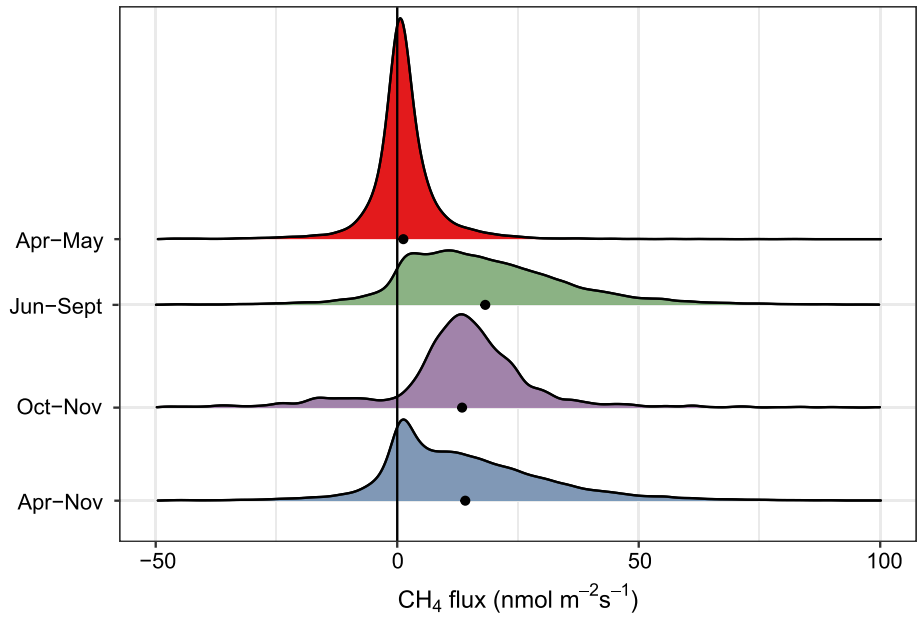

Figure 8. Half-hourly CH_4 flux (nmol m^{-2} s^{-1}) density distribution of all 2013–2019 data separated by April and May (spring), June–September, October and November (fall/freeze-up), and overall April–November distribution. In addition, respective averages (1.11, 18.44, 13.93, and 13.93 nmol m^{-2} s^{-1}) are highlighted as full black circles along the respective *x*-axis.

confident), while 2013 fluxes were significantly lower than those in 2015, but not statistically significantly different from 2016 (see Table S2).

We saw a positive relationship between CH_4 efflux and surface temperature (Figure 9, $r^2 = 0.23$, $p \leq 0.0001$), as well as very high daily average CH_4 fluxes during periods of frequent thawing and refreezing of the surface in July and August. No relationship with amount of precipitation was found.

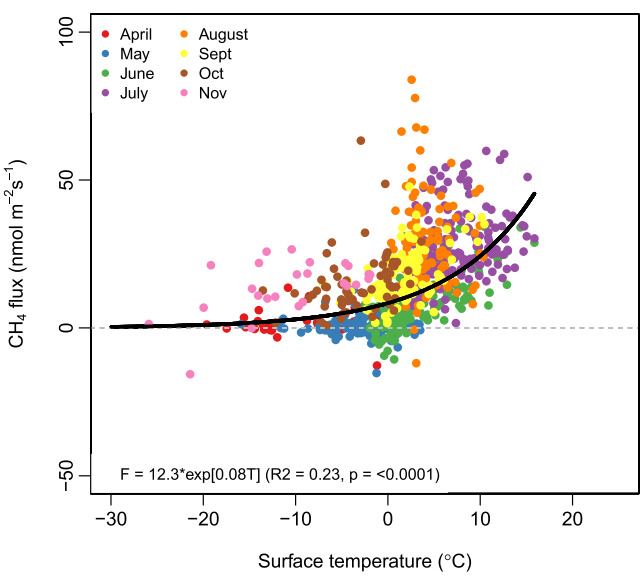

Figure 9. Daily averaged CH_4 fluxes (nmol m^{-2} s^{-1}) measured from April to November, 2013–2019, color coded by month.

Furthermore, CH_4 fluxes correlated with a deepening of the active layer (Figure 10) during the summer month (maximum thaw depth mid-end August) followed by the "zero curtain" (Hinkel et al., 2001) period when the upper surface layer starts to refreeze (data not shown here) but with still substantial CH_4 production in September and the freeze-up season.

3.3. Latent and Sensible Heat Flux

Both latent (LE) and sensible (H) heat showed a decreasing trend over the entire 2013–2019 data collection period ($\tau = -0.121$, $p = 0.001$, $S = -0.01$ W m^{-2} and $\tau = -0.187$, $p \leq 0.0001$, $S = -0.022$ W m^{-2}, respectively), mainly driven by the decrease in the June–September period: June–September average H, for example, declined from 55.24 ($SE = 0.97$) W m^{-2} in 2016 to 23.49 ($SE = 0.44$) W m^{-2} in 2018. Outside this seasonal period, there was a decreasing trend in spring fluxes ($\tau = -0.116$ and -0.127) for both quantities and in fall for H fluxes ($p = 0.0001$) with a change in flux of 0.06 W m^{-2}.

3.4. Climate Variability 2013–2019

There was significant climate variability over the study period in snow-free season dates, rainfall, and temperature. The length of the snow-free season varied from 76 days in 2014 to 159 days in 2016. The variation was due to

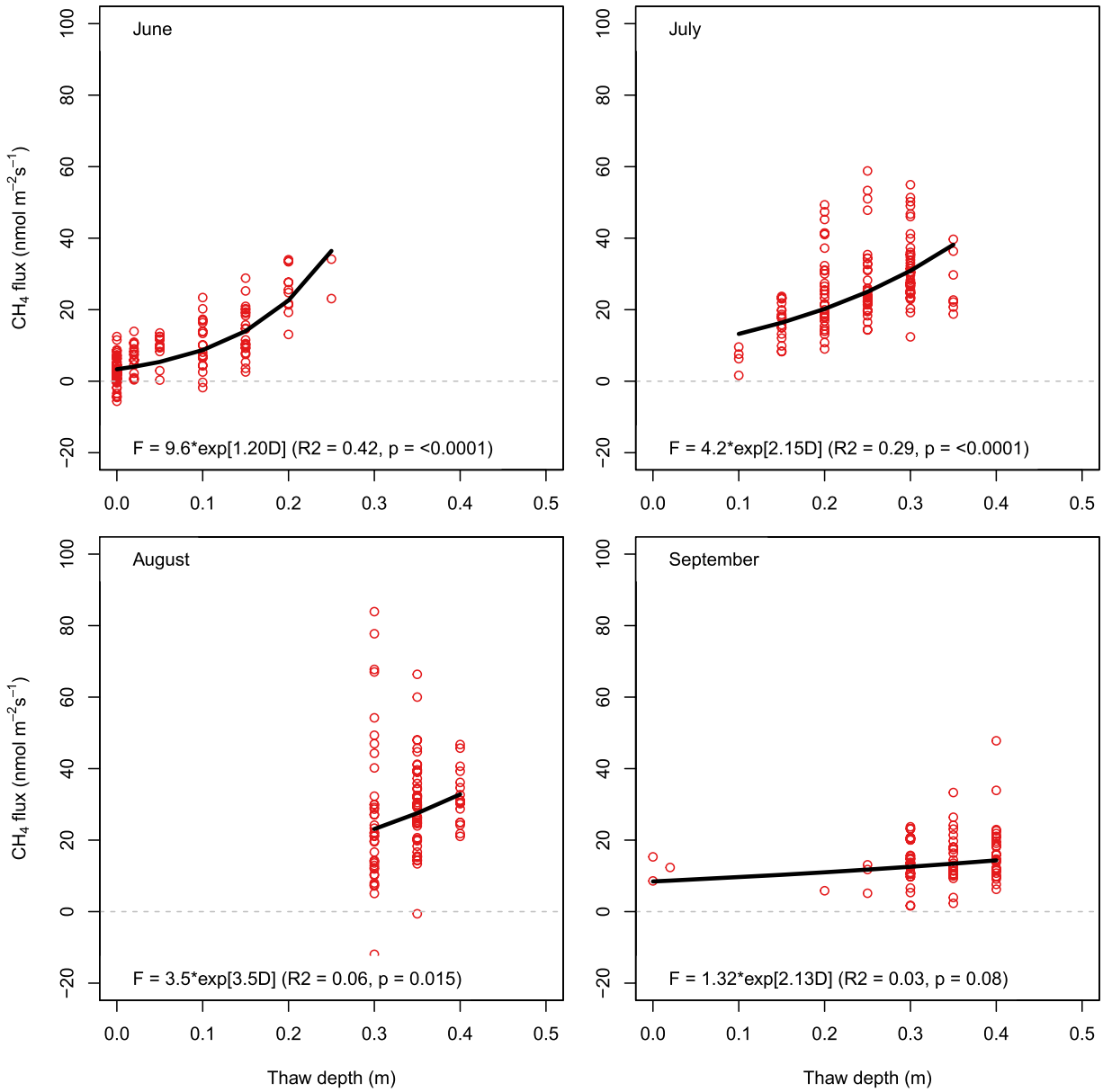

Figure 10. Relationship between daily thaw depths values estimated from soil temperature measurements along a vertical gradient and CH4 fluxes, separated by months.

changes in both snowmelt and accumulation dates. For example, 2016 had the earliest melt (May 24, the record earliest snowmelt since 1902; Cox et al., 2017) and latest autumn accumulation (October 16, record since 1920; Alaska Climate Research Center, 2019; National Weather Service, 2019), while 2018 had the longest-lasting spring snow cover and hence a delayed photosynthetic period. 2016 was also the driest June–September summer season (Table 1), while 2019 had the highest precipitation (176.7 mm, data extracted from the NOAA Barrow Atmospheric Baseline Observatory according to Diamond et al., 2013). In the June–September period each year June was the coldest and July was the warmest month. Although there was high variability among months (see Table 1), the trend across these seven years is that June–September air temperature was slightly increasing (Table S3, $\tau = 0.08$, $p = 0.09$). The 2014 had the coldest and 2019 by far the warmest June–September temperatures (Table 1), representing a record year since 1902 (NOAA, 2019). PPFD, in contrast showed a decreasing trend ($\tau = -0.08$, $p = 0.0002$) with 2019 reporting the highest precipitation values and hence cloudiest conditions.

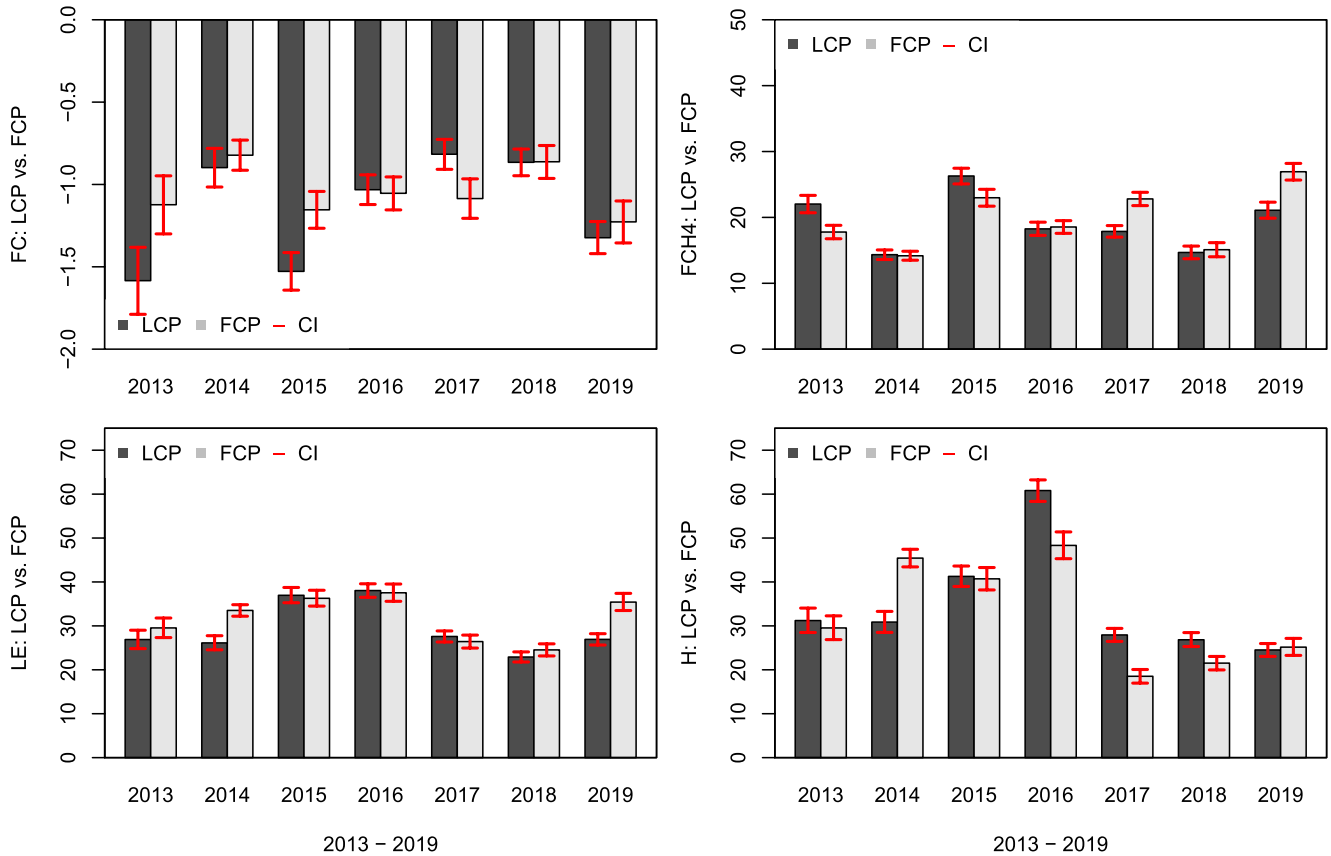

Figure 11. Mean CO_2, CH_4 together with latent (LE) and sensible (H) heat fluxes, together with their respective confidence intervals (CI, in red) at 95% level (including the 2.5th and 97.5th percentile of the bootstrap distribution) after applying bootstrapping (10,000 resamples with replacement) to the data. Represented are low-centered (LCP) and flat-centered (FCP) polygons.

Incoming spring (April and May) radiation (PPDF) showed a very strong increasing trend over the years ($\tau = 0.305$, $p \leq 0.0001$, $S = 0.578$; 2017–2019 were sunnier then previous years and hence warmer spring temperatures), but no significant trend over the October and November fall months. Regarding albedo, no changes were observed over the years.

Spring temperatures increased more than did June–September temperatures ($\tau = 0.104$, $p = 0.045$, $S = 0.01$°C) while the observed increase in October and November temperatures (Table S3) were not significant.

3.5. Attributing Variation in EC Fluxes to Different Polygon Types

To attribute fluxes by polygon type, we mapped the maximum flux-contribution location obtained from our footprint analysis (Figure 2) for April to November, 2013–2019, overlaid on a polygon classification map (see map in Figure 2).

Fluxes varied among polygon types (Figure 11) and the relative flux rates among types changed over time. Measured NEE and CH_4 fluxes from low- and flat-centered polygons can be compared across all June–September periods in Table S5. Within a polygon type, there was no significant trend in spring nor June–September period NEE (Table S3) while during fall months NEE from FCP showed a weak decrease (sign convention for CO_2 fluxes, more negative = more uptake, therefore a positive trend means fluxes are becoming more positive; $p = 0.11$), while the τ value of 0.114 for HCP ($p = 0.19$) hints at a strong decrease in cold season NEE (i.e., less CO_2 uptake). For methane, both polygon types showed a positive trend in June–September CH_4 fluxes (Table S3). There was no detectable trend in spring CH_4 fluxes. Fall CH_4 fluxes, however, exhibited a significant increasing trend in LCPs and marginally significant increasing trend in FCPs.

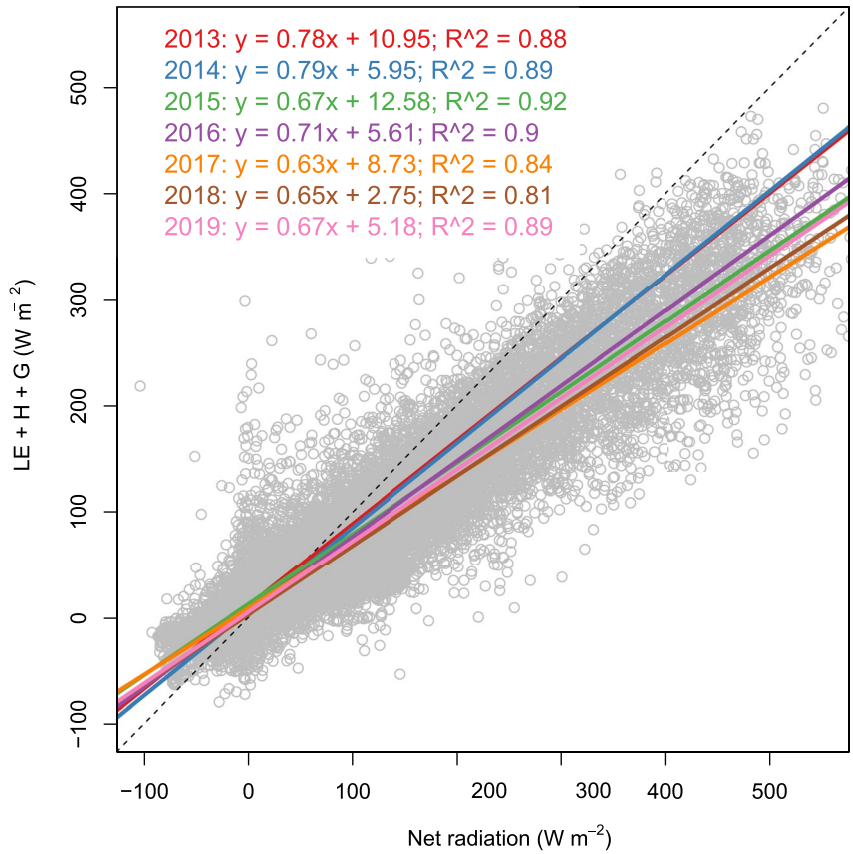

Figure 12. Energy balance for all June–September (2013–2019) data, including net radiation, LE, H, and soil heat flux (G). Added linear regression lines together with the respective functions are color coded by year.

Based on the bootstrapping approach, fluxes across LCP and FCP were not significantly different (at the 95% confidence level) for all June–September periods (Figure 11). Mean CO_2 fluxes in low centered polygons were higher in 2013 and 2015, while in 2017 low centered polygons CO_2 flux means were lower somewhere between 0.12 and 0.42 μmol m^{-2} s^{-1} (Table S6). In contrast, CH_4 fluxes appeared to be significantly different in four out of 7 yr (Figure 11) when comparing low centered with flat centered polygons.

3.6. Energy Fluxes and Energy Balance by Polygon Type

Energy fluxes were similar across the different polygon types in some years and different in others years (Figure 11 and Table S6). For example, latent heat fluxes from low-centered and flat-centered polygons were significantly different in only 2 yr (2014 and 2019, $p < 0.05$). In 2014, June–September average LE from low-centered polygons was 26.11 (SE = 0.81) W m^{-2} compared to 33.5 (SE = 0.67) W m^{-2} over flat-centered polygons. June–September sensible heat values from these polygon types were also significantly different in 2014 and 2016–2018. Notably, 2014 was the only year in which there was no significant difference among LCP and FCP for NEE, GPP, respiration, nor for CH_4 fluxes. LE and H, decreased over the study period (Table 1).

Considering all June–September data (Figure 12), energy balance ((LE-H + G)/net radiation) averaged 70% with large fluctuations among polygon types, years, and months (range 35%–94%). Such energy balance estimates at EC sites include uncertainties introduced by the lack of representativeness of net radiation and soil heat flux measurements (fixed point measurements) in the wider area near the eddy flux tower (change in footprint, regarding LE and H), as well as lateral energy losses via subsurface water flows.

No significant difference in energy balance closure was found amongst the different polygons in any year. Across years, however, energy balance closure sharply increased for the spring months ($\tau = 0.24$, $p \leq 0.0001$) but no significant trend in the June–September nor the fall/freeze-up period was observed.

One uncertainty we found in energy balance measurements at our site were the behavior of ground heat fluxes over the years. The two continuously running soil heat flux plates (both in LCP) showed no trend in the spring but opposing trends during June–September ($\tau = -0.09$, $p = 0.06$ and $\tau = 0.101$, $p = 0.02$) and clear increasing trends in the fall months ($\tau = 0.193$ and 0.109) with only one being weakly significant ($p = 0.07$).

4. Discussion

Fluxes of CO_2, CH_4, and energy over 7 yr (2013–2019), including early spring/snowmelt (April and May), June–September and the post photosynthetic period/freeze-up season (October and November) from a polygon tundra, EC flux site near Utqiagvik, Alaska are discussed here. An overview of the meteorological conditions and flux distribution shows inter- and intra-seasonal variation but also notable spatial variability in partitioned flux values.

4.1. CO_2 Fluxes

The timing of snowmelt and spring temperatures had a large impact on tundra carbon sequestration. While the cumulative sink by the beginning of August 2018 was only 50 g C m^{-2} (Figure 5), in 2015 (snow-free since May and with the warmest spring temperatures of the 7 yr [Table 1]), approximately twice as much carbon was sequestered. This said, 2016, the year with the longest snow-free season but lowest precipitation values had intermediate carbon uptake (see Figure 5). The snow free season in 2017 and 2018 commenced 3 days apart in late June and lasted in both years until 29 September with 2017 having sequestered 30 g C m^{-2} more than in 2018. The 2015 and 2019 showed a decline in uptake throughout September though the tundra remained snow free until 22 September in 2015 and until 9 October in 2019, respectively. Both years had 117 and 121 snow free days, respectively accumulating between 101 and 104 g C m^{-2}. In contrast 2016, the longest snow free season with 159 days sequestered only 73 g C m^{-2} by the end of August.

Our findings show no trend in CO_2 uptake linked to snow-free season length, an observation also made in High Arctic Siberia by Parmentier et al. (2011) from 8 consecutive years of CO_2 EC flux measurements.

The tundra was a net CO_2 sink in every of the seven June–September periods, driven by summer uptake (Figure 5) at rates similar to those measured by Euskirchen et al. (2012) for Imnavait Creek in the northern foothills of the Brooks Range, Alaska, but slightly lower than 119 g m^{-2} June–August average in the Lena Delta, Siberia (Kutzbach et al., 2007). Net CO_2 uptake commenced shortly after snowmelt, when air temperatures are still relatively low but insolation levels are highest, thus favoring GPP over soil respiration. The strong influence of PPFD (Figure 6) on Arctic GPP has been documented with EC in high-Arctic polygon tundra in Siberia (Dennis et al., 1978; Kutzbach et al., 2007) and at leaf level at our site (Rogers et al., 2019). Ecosystem respiration increased exponentially with surface temperature (Figure 7), as seen in other studies at the BEO (Harazono et al., 2003; Oechel et al., 1995) and Lena Delta (Kutzbach et al., 2007).

4.2. Changes in CH_4 Fluxes Over Time

June–September CH_4 fluxes showed an increasing trend (Mann-Kendall analysis) between 2013 and 2019, in concert with a slight increase in June–September air temperature (Table S3) and a potential deepening of the active layer (measurements near the site are done in up to 5 cm increments up to a depth of 0.4 m and 10–20 cm increments from 0.4 m downward, see Figure 10). The strong link with air and/or soil surface temperature (Figure 9) was also found in other Arctic studies (Arndt et al., 2019; Friborg et al., 2000; Sachs et al., 2010; Wille et al., 2008; Zona, Oechel, Kochendorfer, et al., 2009). Generally Arctic tundra soil temperatures at deeper depths vary too little (thermal inertia) however, to explain the high variability in CH_4 fluxes. Zona et al. (2016) and Taylor et al. (2018) estimated that around half of annual Arctic CH_4 emissions occur outside the snow-free season, with substantial contributions during freeze-up (Mastepanov et al., 2008; Pirk et al., 2015; Tagesson et al., 2012) and spring thaw (Raz-Yaseef et al., 2017; Wille et al., 2008) originating from individual pulse events, a phenomenon also observed in boreal permafrost regions (Hargreaves et al., 2001; Song et al., 2012). We observed large CH_4 fluxes during freeze-up in all years (Figures 3, 8, and 9), and substantial spring-thaw pulses only in 2014 (Raz-Yaseef et al., 2017).

4.3. Spatial Heterogeneity of Tundra Fluxes

Inundated areas, ponds, and lakes in high-latitude tundra can act as hotspots for both CO_2 and CH_4 fluxes (Jammet et al., 2015, 2017; Langer et al., 2015), contributing to the spatial heterogeneity of high-latitude greenhouse gas fluxes. In addition, studies of vegetated drained thaw lake basins (DTLBs) near Utqiagvik found that the age of the basins (i.e., time since lake drainage) affects flux rates too (Lara et al., 2015; Sturtevant & Oechel, 2013), with higher NEE and GPPs in young DTLBs (Lara et al., 2015; Zona, Oechel, Peterson, et al., 2009). Changes in land cover type, age, permafrost thaw, and wetter or drier areas have a potential to impact future polygon tundra properties and fluxes in a warming climate (Lara et al., 2015, 2018).

4.4. Impact of Polygonal Features on Tundra Greenhouse Gases

What impact do polygonal features have on tundra greenhouse gases? NEE fluxes from the two dominant polygon types, low- and flat-centered polygons, were significantly different during only three years (Figure 11). Regarding CH_4 fluxes, in the first 3 yr (2013–2015) moister LCPs had higher fluxes (Table S5), followed by 4 yr (2016–2019) in which FCPs had higher values, with the increase in FCP CH_4 fluxes partially explained by an increase in seasonal air temperature ($p < 0.001$) and variation in precipitation ($p = 0.067$) dynamics, both promoting a deepening of the active layer (Douglas et al., 2020).

Polygon type alone did not explain the differences in fluxes. In addition, snow cover distribution is not uniform in these ecosystems (Gouttevin et al., 2018; Kępski et al., 2017; Wainwright et al., 2017), with snow depth during the first half of the June–September period potentially being more persistent in low-centered polygons than in flat- or high-centered polygons (Zona, Oechel, Kochendorfer, et al., 2009).

The result could be that due to wind and snow drift insulating the soil and exposing some flux drivers much later in the season than in drier high- and flat-centered polygons, thus contributing to differences in fluxes among polygon types. This also applies to spatially changing soil temperatures in the upper most layers of the tundra soil during snow melt, as well as the "zero-curtain" (Hinkel et al., 2001) effect later in the season.

4.5. Gas and Energy Fluxes at Polygon Level

This is the first study to attribute eddy fluxes to different polygon types in the footprint. Chamber data can provide an independent check on the relative patterns we found. Studies near our site (Lara et al., 2015; Sturtevant & Oechel, 2013; Vaughn et al., 2016; von Fischer et al., 2010; Wainwright et al., 2015) and in Siberian polygon tundra (Sachs et al., 2010; Wagner et al., 2003) report higher CH_4 fluxes from low-centered polygons than from drier areas such as high- and flat-centered polygons. These studies also found high fluxes from wetter features within the polygon landscape, such as depressions and troughs compared to the drier rims, but these fine-scale variations cannot be resolved by EC data. Studies have also found high CH_4 fluxes from the normally drier FCPs during wetter periods, consistent with our observations of the impact of an increase in precipitation.

The Arctic tundra not only shows a high spatial heterogeneity in greenhouse gas flux but also in surface energy fluxes (Boike et al., 2008; Langer et al., 2011; Lynch, Bonan et al., 1999; Muster et al., 2012; Ohmura, 1981, 1982), an interplay between climate drivers (e.g., available radiation/meteorological conditions) and ecosystem properties (soil, hydrology or wetness, and vegetation cover; Ling & Zhang, 2004; Sedighi et al., 2018). Our estimation of the site energy balance was problematic, as it is for nearly all EC systems, due to a mismatch in spatial scale in different measurements. While outgoing radiation and soil heat flux were estimated as fixed point measurements, turbulent fluxes were averaged over larger areas with a changing footprint, and influenced by microtopographical features, dry versus wet areas, and lateral losses of energy. Nevertheless, our half-hourly energy balance values (mostly above 60%, range 35%–94%) were within the ranges found in other energy balance studies in the High Arctic (Lynch, Bonan, et al., 1999 and authors therein; Grachev et al., 2019; Langer et al., 2011; Lund et al., 2014).

4.6. Heterogeneity of Polygon Tundra and Land-Surface Models

The heterogeneity of polygon tundra poses a challenge to land-surface models, predictions, and model fidelity. For example, a comparison of 40 models (Fisher et al., 2014) as well as a newer comparison study of 11 models

by Commane et al. (2017) showed that the spatial patterns in mean NEE for Alaska varied widely among models, essentially showing no consistent distribution and some models completely contradicting the outcome from other models. A model study of energy fluxes limited to the North Slope of Alaska (Lynch, Bonan et al., 1999; Lynch, Chapin, et al., 1999) detailed the difficulty of model validation and performance using data measured at multiple sites across similar terrain by multiple research groups, highlighting the uncertainties attached to measurement methods and instruments used. Model input affected model outputs by under/over estimating individual land cover features (Wainwright et al., 2015), flux components (Grant, Mekonnen, Riley, Wainwright, et al., 2017), and fluxes (Grant et al., 2019; Grant, Mekonnen, Riley, Arora, & Torn, 2017), ultimately illustrating the complexity of small-scale variations of the greenhouse gas and energy balance in ecosystem processes at regional scales. These numerous studies and models highlight the lack of complete understanding of the complex and heterogeneous Arctic polygon tundra, its dynamics, and future development under a changing climate.

5. Conclusion

Seven years of CO_2, CH_4, and energy fluxes (April to November, 2013–2019) revealed an increasing trend in CH_4 fluxes from Arctic tundra, including increasing fall (freeze up) fluxes as well as a consistent CO_2 sink during June to September months in each year, at the Barrow Ecological Observatory near Utqiagvik Alaska. There was high temporal and spatial variability in NEE, CH_4, LE, and H fluxes linked to climate variability and site heterogeneity. To disentangle the heterogeneity of the complex polygonal tundra, we combined a polygon type classification (Wainwright et al., 2015) and footprint analysis that allowed us to separate the maximum flux-contribution location by polygon type. It revealed which polygon type had higher NEE or CH_4 fluxes that varied by time period investigated and year. Multi-year, multi-season data were necessary to quantify the long term trends and the relationship between spatial patterns (e.g., among polygon types) and climate variability. We hope this approach will pave the way for further such studies, extending understanding of the heterogeneity of Arctic ecosystems and the use of flux data in land model development, parameterization and validation.

Data Availability Statement

All eddy covariance and meteorological data included in this study are freely obtainable from the AmeriFlux database (https://ameriflux.lbl.gov/data/data-availability/) and additional auxiliary data from the US Department of Energy Next-Generation Ecosystem Experiments (NGEE Arctic) Data Portal (https://ngee-arctic.ornl.gov/data/).

Acknowledgments
The Next-Generation Ecosystem Experiments (NGEE Arctic) project is supported by the Office of Biological and Environmental Research in the US Department of Energy Office of Science.

References

Aalto, J., Scherrer, D., Lenoir, J., Guisan, A., & Luoto, M. (2018). Biogeophysical controls on soil-atmosphere thermal differences: Implications on warming Arctic ecosystems. *Environmental Research Letters*, *13*(7), 074003. https://doi.org/10.1088/1748-9326/aac83e

Alaska Climate Research Center. (2019). University of Alaska Fairbanks. Retrieved from http://akclimate.org/

Andresen, C. G., Lawrence, D. M., Wilson, C. J., McGuire, A. D., Koven, C., Schaefer, K., et al. (2020). Soil moisture and hydrology projections of the permafrost region—A model intercomparison. *The Cryosphere*, *14*, 445–459. https://doi.org/10.5194/tc-14-445-2020

Arndt, K. A., Oechel, W. C., Goodrich, J. P., Bailey, B. A., Kalhori, A., Hashemi, J., et al. (2019). Sensitivity of methane emissions to later soil freezing in Arctic tundra ecosystems. *Journal of Geophysical Research: Biogeosciences*, *124*(8), 2595–2609. https://doi.org/10.1029/2019jg005242

Aubinet, M., Vesala, T., & Papale, D. (Eds.). (2012). *Eddy covariance: A practical guide to measurement and data analysis*. Springer, Springer Atmospheric Sciences.

Baldocchi, D. D. (2003). Assessing the eddy covariance technique for evaluating carbon dioxide exchange rates of ecosystems: Past, present and future. *Global Change Biology*, *9*(4), 479–492. https://doi.org/10.1046/j.1365-2486.2003.00629.x

Baldocchi, D. D., Hincks, B. B., & Meyers, T. P. (1988). Measuring biosphere-atmosphere exchanges of biologically related gases with micrometeorological methods. *Ecology*, *69*(5), 1331–1340. https://doi.org/10.2307/1941631

Banjanovic, E. S., & Osborne, J. W. (2016). Confidence intervals for effect sizes: Applying bootstrap resampling. *Practical Assessment, Research and Evaluation*, *21*(1), 5. https://doi.org/10.7275/dz3r-8n08

Belshe, E. F., Schuur, E. A. G., & Bolker, B. M. (2013). Tundra ecosystems observed to be CO2 sources due to differential amplification of the carbon cycle. *Ecology Letters*, *16*(10), 1307–1315. https://doi.org/10.1111/ele.12164

Biskaborn, B. K., Smith, S. L., Noetzli, J., Matthes, H., Vieira, G., Streletskiy, D. A., et al. (2019). Permafrost is warming at a global scale. *Nature Communications*, *10*(1), 1–11. https://doi.org/10.1038/s41467-018-08240-4

Bockheim, J. G., Everett, L. R., Hinkel, K. M., Nelson, F. E., & Brown, J. (1999). Soil organic carbon storage and distribution in Arctic tundra, Barrow, Alaska. *Soil Science Society of America Journal*, *63*(4), 934–940. https://doi.org/10.2136/sssaj1999.634934x

Boike, J., Wille, C., & Abnizova, A. (2008). Climatology and summer energy and water balance of polygonal tundra in the Lena River Delta, Siberia. *Journal of Geophysical Research*, *113*(G3). https://doi.org/10.1029/2007jg000540

Box, J. E., Colgan, W. T., Christensen, T. R., Schmidt, N. M., Lund, M., Parmentier, F. J. W., et al. (2019). Key indicators of Arctic climate change: 1971–2017. *Environmental Research Letters*, *14*(4), 045010. https://iopscience.iop.org/article/10.1088/1748-9326/aafc1b

Brown, J. (1967). Tundra soils formed over ice wedges, northern Alaska. *Soil Science Society of America Journal*, *31*(5), 686–691. https://doi.org/10.2136/sssaj1967.03615995003100050022x

Burba, G. G. (2001). Illustration of flux footprint estimates affected by measurement height, surface roughness and thermal stability. In Hubbards, K. & Sivakumar, M. (Eds.), *Automated Weather Stations for Applications in Agriculture and Water Resources Management: Current Use and Future Perspectives* (pp. 77–86). World Meteorological Organization.

Burba, G. G. (2013). *Eddy covariance method for scientific, industrial, agricultural and regulatory applications: A field book on measuring ecosystem gas exchange and areal emission rates*. LI-COR Biosciences.

Causton, D. R., & Dale, M. P. (1990). The monomolecular and rectangular hyperbola as empirical models of the response of photosynthetic rate to photon flux density, with applications to three Veronica species. *Annals of Botany*, *65*(4), 389–394. https://doi.org/10.1093/oxfordjournals.aob.a087949

Cherry, J., & Crowder, K. (2016). Airborne imagery collections Barrow 2013. Next generation ecosystem experiments Arctic data collection [Data set]. Oak Ridge National Laboratory, U.S. Department of Energy. https://doi.org/10.5440/1167159

Christianson, D. S., Beekwilder, N., Chan, S., Cheah, Y. W., Chu, H., Dengel, S., et al. (2017). AmeriFlux data processing: Integrating automated and manual data management across software technologies and an international network to generate timely data products. In *Proceeding 50th AGU Annual Fall Meeting*, American Geophysical Union.

Commane, R., Lindaas, J., Benmergui, J., Luus, K. A., Chang, R. Y. W., Daube, B. C., et al. (2017). Carbon dioxide sources from Alaska driven by increasing early winter respiration from Arctic tundra. *Proceedings of the National Academy of Sciences of the United States of America*, *114*(21), 5361–5366. https://doi.org/10.1073/pnas.1618567114

Cox, C. J., Stone, R. S., Douglas, D. C., Stanitski, D. M., Divoky, G. J., Dutton, G. S., et al. (2017). Drivers and environmental responses to the changing annual snow cycle of northern Alaska. *Bulletin of the American Meteorological Society*, *98*(12), 2559–2577. https://doi.org/10.1175/bams-d-16-0201.1

Cristóbal, J., Prakash, A., Anderson, M. C., Kustas, W. P., Euskirchen, E. S., & Kane, D. L. (2017). Estimation of surface energy fluxes in the Arctic tundra using the remote sensing thermal-based two-source energy balance model. *Hydrology and Earth System Sciences*, *21*(3), 1339–1358.

Dai, X. G., & Wang, P. (2018). Identifying the early 2000s hiatus associated with internal climate variability. *Scientific Reports*, *8*(1), 1–13. https://doi.org/10.1038/s41598-018-31862-z

Dengel, S., Billesbach, D., & Torn, M. (2020). NGEE Arctic CO2, CH4 and energy eddy-covariance (EC) flux tower auxiliary measurements, Utqiagvik (Barrow), Alaska, 2012—Ongoing. Next generation ecosystem experiments Arctic data collection [Data set]. Oak Ridge National Laboratory, U.S. Department of Energy. https://doi.org/10.5440/1362279

Dennis, J. G., Tieszen, L. L., & Vetter, M. A. (1978). Seasonal dynamics of above-and belowground production of vascular plants at Barrow, Alaska. In Tieszen, L. L. (Ed.), *Vegetation and production ecology of an Alaskan Arctic tundra. Ecological Studies (Analysis and Synthesis)* (Vol. 29, pp. 113–140). Springer. https://doi.org/10.1007/978-1-4612-6307-4_4

de Vrese, P., Stacke, T., Kleinen, T., & Brovkin, V. (2021). Diverging responses of high-latitude CO2 and CH4 emissions in idealized climate change scenarios. *The Cryosphere*, *15*, 1097–1130. https://doi.org/10.5194/tc-15-1097-2021

Diamond, H. J., Karl, T. R., Palecki, M. A., Baker, C. B., Bell, J. E., Leeper, R. D., et al. (2013). US Climate Reference Network after one decade of operations: Status and assessment. *Bulletin of the American Meteorological Society*, *94*, 485–498. https://doi.org/10.1175/bams-d-12-00170.1

Douglas, T. A., Turetsky, M. R., & Koven, C. D. (2020). Increased rainfall stimulates permafrost thaw across a variety of Interior Alaskan boreal ecosystems. *NPJ Climate and Atmospheric Science*, *3*, 28. https://doi.org/10.1038/s41612-020-0130-4

Euskirchen, E. S., Bret-Harte, M. S., Scott, G. J., Edgar, C., & Shaver, G. R. (2012). Seasonal patterns of carbon dioxide and water fluxes in three representative tundra ecosystems in northern Alaska. *Ecosphere*, *3*(1), 1–19. https://doi.org/10.1890/es11-00202.1

Euskirchen, E. S., Bret-Harte, M. S., Shaver, G. R., Edgar, C. W., & Romanovsky, V. E. (2017). Long-term release of carbon dioxide from Arctic tundra ecosystems in Alaska. *Ecosystems*, *20*(5), 960–974. https://doi.org/10.1007/s10021-016-0085-9

Euskirchen, E. S., Carman, T. B., & McGuire, A. D. (2014). Changes in the structure and function of northern Alaskan ecosystems when considering variable leaf-out times across groupings of species in a dynamic vegetation model. *Global Change Biology*, *20*(3), 963–978. https://doi.org/10.1111/gcb.12392

Fisher, J. B., Sikka, M., Oechel, W. C., Huntzinger, D. N., Melton, J. R., Koven, C. D., et al. (2014). Carbon cycle uncertainty in the Alaskan Arctic. *Biogeosciences*, *11*, 4271–4288. https://doi.org/10.5194/bg-11-4271-2014

Foken, T., Göockede, M., Mauder, M., Mahrt, L., Amiro, B., & Munger, W. (2004). Post-field data quality control. In Lee, X., Massman, W., & Law, B. (Eds.), *Handbook of micrometeorology* (pp. 181–208). Springer. https://doi.org/10.1007/1-4020-2265-4_9

Fox, A. M., Huntley, B., Lloyd, C. R., Williams, M., & Baxter, R. (2008). Net ecosystem exchange over heterogeneous Arctic tundra: Scaling between chamber and eddy covariance measurements. *Global Biogeochemical Cycles*, *22*(2). https://doi.org/10.1029/2007gb003027

Friborg, T., Christensen, T. R., Hansen, B. U., Nordstroem, C., & Soegaard, H. (2000). Trace gas exchange in a high-Arctic valley: 2. Landscape CH4 fluxes measured and modeled using eddy correlation data. *Global Biogeochemical Cycles*, *14*(3), 715–723. https://doi.org/10.1029/1999gb001136

Gewirtzman, J., Tang, J., Parker, T. & Fetcher, N. (2018). Soil drying and active layer deepening decrease productivity across ecotypes of a dominant Arctic sedge. *Presented at AGU 2018 Annual Fall Meeting*. https://www.essoar.org/doi/abs/10.1002/essoar.10500831.1

Gouttevin, I., Langer, M., Löwe, H., Boike, J., Proksch, M., & Schneebeli, M. (2018). Observation and modelling of snow at a polygonal tundra permafrost site: Spatial variability and thermal implications. *The Cryosphere*, *12*(11), 3693–3717. https://doi.org/10.5194/tc-12-3693-2018

Grachev, A. A., Fairall, C. W., Blomquist, B. W., Fernando, H. J., Leo, L. S., Otárola-Bustos, S. F., et al. (2019). On the surface energy balance closure at different temporal scales. *Agricultural and Forest Meteorology*, *281*, 1078232. https://doi.org/10.1016/j.agrformet.2019.107823

Graham, D. E., Roy Chowdhury, T., Herndon, E., Chourey, K., Ladd, M., Tas, N., et al. (2013). Biogeochemical controls on microbial CO_2 and CH_4 production in interstitial area polygon soils from the Barrow Environmental Observatory. *Poster presented at the 2013 AGU Annual Fall Meeting*.

Grant, R. F., Mekonnen, Z. A., Riley, W. J., Arora, B., & Torn, M. S. (2017). Mathematical modelling of Arctic polygonal tundra with ecosys: 2. Microtopography determines how CO2 and CH4 exchange responds to changes in temperature and precipitation. *Journal of Geophysical Research: Biogeosciences*, *122*(12), 3174–3187. https://doi.org/10.1002/2017jg004037

Grant, R. F., Mekonnen, Z. A., Riley, W. J., Arora, B., & Torn, M. S. (2019). Modeling climate change impacts on an Arctic polygonal tundra: 2. Changes in CO2 and CH4 exchange depend on rates of permafrost thaw as affected by changes in vegetation and drainage. *Journal of Geophysical Research: Biogeosciences*, *124*(5), 1323–1341. https://doi.org/10.1029/2018jg004645

Grant, R. F., Mekonnen, Z. A., Riley, W. J., Wainwright, H. M., Graham, D., & Torn, M. S. (2017). Mathematical modelling of Arctic polygonal tundra with ecosys: 1. Microtopography determines how active layer depths respond to changes in temperature and precipitation. *Journal of Geophysical Research: Biogeosciences*, *122*(12), 3161–3173. https://doi.org/10.1002/2017jg004035

Grøndahl, L., & Ministry of the Environment-Denmark. (2006). *Carbon dioxide exchange in the high Arctic: Examples from terrestrial ecosystems* [Doctoral dissertation, Faculty of Science, Institute of Geography, University of Copenhagen]. National Environmental Research Institute. https://www2.dmu.dk/Pub/phd_lgr.pdf

Hamed, K. H. & Rao, A. R. (1998). A modified Mann-Kendall trend test for autocorrelated data. *Journal of Hydrology*, *204*(1–4), 182–196. https://doi.org/10.1016/s0022-1694(97)00125-x

Harazono, Y., Mano, M., Miyata, A., Kwon, H., & Oechel, W. C. (2003). Annual CO2 budget at Arctic wet sedge tundra in Barrow and the contribution of winter fluxes. *AGUFM*, B52D–B06.

Hargreaves, K. J., Fowler, D., Pitcairn, C. E. R., & Aurela, M. (2001). Annual methane emission from Finnish mires estimated from eddy covariance campaign measurements. *Theoretical and Applied Climatology*, *70*(1–4), 203–213. https://doi.org/10.1007/s007040170015

Hinkel, K. M., Paetzold, F., Nelson, F. E., & Bockheim, J. G. (2001). Patterns of soil temperature and moisture in the active layer and upper permafrost at Barrow, Alaska: 1993-1999. *Global and Planetary Change 29*(3–4):293–309. https://doi.org/10.1016/s0921-8181(01)00096-0

Hugelius, G., Loisel, J., Chadburn, S., Jackson, R. B., Jones, M., MacDonald, G., et al. (2020). Large stocks of peatland carbon and nitrogen are vulnerable to permafrost thaw. *Proceedings of the National Academy of Sciences of the United States of America*, *117*(34), 20438–20446. https://doi.org/10.1073/pnas.1916387117

Jammet, M., Crill, P., Dengel, S., & Friborg, T. (2015). Large methane emissions from a subarctic lake during spring thaw: Mechanisms and landscape significance. *Journal of Geophysical Research: Biogeosciences*, *120*(11), 2289–2305. https://doi.org/10.1002/2015jg003137

Jammet, M., Dengel, S., Kettner, E., Parmentier, F. J. W., Wik, M., Crill, P., & Friborg, T. (2017). Year-round CH4 and CO2 flux dynamics in two contrasting freshwater ecosystems of the subarctic. *Biogeosciences*, *14*, 5189–5216. https://doi.org/10.5194/bg-14-5189-2017

Jansson, J. K., Tas, N., Brodie, E. L., Graham, D. E., Kneafsey, T. J., Torn, M. S., et al. (2012). Horizontal and vertical profiling of microbial communities across landscape features at NGEE site, Barrow, Alaska. In *Paper presented at the 2012 Fall Meeting (Abstract C31C-06)*. American Geophysical Union.

Jeong, S. J., Bloom, A. A., Schimel, D., Sweeney, C., Parazoo, N. C., Medvigy, D., et al. (2018). Accelerating rates of Arctic carbon cycling revealed by long-term atmospheric CO2 measurements. *Science Advances*, *4*(7), eaao1167. https://doi.org/10.1126/sciadv.aao1167

Kaimal, J. C., & Gaynor, J. E. (1991). Another look at sonic thermometry. *Boundary-Layer Meteorology*, *56*(4), 401–410. https://doi.org/10.1007/bf00119215

Keenan, T. F., Migliavacca, M., Papale, D., Baldocchi, D., Reichstein, M., Torn, M., & Wutzler, T. (2019). Widespread inhibition of daytime ecosystem respiration. *Nature Ecology & Evolution*, *3*(3), 407–415. https://doi.org/10.1038/s41559-019-0809-2

Kendall, M. (1975). *Rank correlation measures* (p. 15). Charles Griffin.

Kępski, D., Luks, B., Migała, K., Wawrzyniak, T., Westermann, S., & Wojtuń, B. (2017). Terrestrial remote sensing of snowmelt in a diverse High-Arctic tundra environment using time-lapse imagery. *Remote Sensing*, *9*(7), 733.

Keuper, F., Wild, B., Kummu, M., Beer, C., Blume-Werry, G., Fontaine, S., et al. (2020). Carbon loss from northern circumpolar permafrost soils amplified by rhizosphere priming. *Nature Geoscience*, *13*(8), 560–565. https://doi.org/10.1038/s41561-020-0607-0

Kljun, N., Calanca, P., Rotach, M. W., & Schmid, H. P. (2004). A simple parameterisation for flux footprint predictions. *Boundary-Layer Meteorology*, *112*(3), 503–523. https://doi.org/10.1023/b:boun.0000030653.71031.96

Kormann, R., & Meixner, F. X. (2001). An analytical footprint model for non-neutral stratification. *Boundary-Layer Meteorology*, *99*(2), 207–224. https://doi.org/10.1023/a:1018991015119

Koven, C. D., Lawrence, D. M., & Riley, W. J. (2015). Permafrost carbon − Climate feedback is sensitive to deep soil carbon decomposability but not deep soil nitrogen dynamics. *Proceedings of the National Academy of Sciences of the United States of America*, *112*(12), 3752–3757. https://doi.org/10.1073/pnas.1415123112

Kutzbach, L. (2006). *The exchange of energy, water and carbon dioxide between wet Arctic tundra and the atmosphere at the Lena River Delta, Northern Siberia = Der Austausch von Energie, Wasser und Kohlendioxid zwischen arktischer Feuchtgebiets-Trundra und der Atmosphäre im nordsibirischen Lena Delta. [Berichte zur Polar-und Meeresforschung (Reports on Polar and Marine Research)]*, p. 541. https://doi.org/10.2312/BZPM_0541_2006

Kutzbach, L., Wille, C., & Pfeiffer, E. M. (2007). The exchange of carbon dioxide between wet Arctic tundra and the atmosphere at the Lena River Delta, Northern Siberia. *Biogeosciences*, *4*, 869–890.

Langer, M., Westermann, S., Muster, S., Piel, K., & Boike, J. (2011). The surface energy balance of a polygonal tundra site in northern Siberia–Part 1: Spring to fall. *The Cryosphere*, *5*(1), 151–171. https://doi.org/10.5194/tc-5-151-2011

Langer, M., Westermann, S., Walter Anthony, K., Wischnewski, K., & Boike, J. (2015). Frozen ponds: Production and storage of methane during the Arctic winter in a lowland tundra landscape in northern Siberia, Lena River delta. *Biogeosciences*, *12*(4), 977–990. https://doi.org/10.5194/bg-12-977-2015

Lara, M. J., McGuire, A. D., Euskirchen, E. S., Tweedie, C. E., Hinkel, K. M., Skurikhin, A. N., et al. (2015). Polygonal tundra geomorphological change in response to warming alters future CO 2 and CH 4 flux on the Barrow Peninsula. *Global Change Biology*, *21*(4), 1634–1651. https://doi.org/10.1111/gcb.12757

Lara, M. J., Nitze, I., Grosse, G., Martin, P., & McGuire, A. D. (2018). Reduced Arctic tundra productivity linked with landform and climate change interactions. *Scientific Reports*, *8*(1), 1–10. https://doi.org/10.1038/s41598-018-20692-8

LI-COR. (2010). *LI-7700 open path CH4 analyzer instruction manual*. LI-COR Biosciences. https://www.licor.com/env/support/LI-7700/manuals.html

Liljedahl, A. K., Boike, J., Daanen, R. P., Fedorov, A. N., Frost, G. V., Grosse, G., et al. (2016). Pan-Arctic ice-wedge degradation in warming permafrost and its influence on tundra hydrology. *Nature Geoscience*, *9*(4), 312–318. https://doi.org/10.1038/ngeo2674

Ling, F., & Zhang, T. (2004). A numerical model for surface energy balance and thermal regime of the active layer and permafrost containing unfrozen water. *Cold Regions Science and Technology*, *38*(1), 1–15. https://doi.org/10.1016/s0165-232x(03)00057-0

Lloyd, J., & Taylor, J. A. (1994). On the temperature dependence of soil respiration. *Functional Ecology*, *8*(3), 315–323. https://doi.org/10.2307/2389824

López-Blanco, E., Lund, M., Williams, M., Tamstorf, M. P., Westergaard-Nielsen, A., Exbrayat, J. F., et al. (2017). Exchange of CO_2 in Arctic tundra: Impacts of meteorological variations and biological disturbance. *Biogeosciences*, *14*(19), 4467–4483. https://doi.org/10.5194/bg-14-4467-2017

Lund, M., Hansen, B. U., Pedersen, S. H., Stiegler, C., & Tamstorf, M. P. (2014). Characteristics of summer-time energy exchange in a high Arctic tundra heath 2000–2010. *Tellus B: Chemical and Physical Meteorology*, *66*(1), 21631. https://doi.org/10.3402/tellusb.v66.21631

Lynch, A. H., Bonan, G. B., Chapin, F. S. III, & Wu, W. (1999). Impact of tundra ecosystems on the surface energy budget and climate of Alaska. *Journal of Geophysical Research: Atmospheres*, *104*(D6), 6647–6660. https://doi.org/10.1029/98jd02798

Lynch, A. H., Chapin, F. S. III, Hinzman, L. D., Wu, W., Lilly, E., Vourlitis, G., & Kim, E. (1999). Surface energy balance on the Arctic tundra: Measurements and models. *Journal of Climate*, *12*(8), 2585–2606. https://doi.org/10.1175/1520-0442(1999)012<2585:sebota>2.0.co;2

Lyu, Z. (2015). *The role of snow in soil thermal dynamics of the Arctic terrestrial ecosystems* [Doctoral dissertation]. Purdue University. https://docs.lib.purdue.edu/open_access_theses/1222

Lyu, Z., & Zhuang, Q. (2018). Quantifying the effects of snowpack on soil thermal and carbon dynamics of the Arctic terrestrial ecosystems. *Journal of Geophysical Research: Biogeosciences*, *123*(4), 1197–1212. https://doi.org/10.1002/2017jg003864

Mann, H. B. (1945). Nonparametric tests against trend. *Econometrica*, *13*(3), 245–259. https://doi.org/10.2307/1907187

Massman, W. J. (2000). A simple method for estimating frequency response corrections for eddy covariance systems. *Agricultural and Forest Meteorology*, *104*(3), 185–198. https://doi.org/10.1016/s0168-1923(00)00164-7

Mastepanov, M., Sigsgaard, C., Dlugokencky, E. J., Houweling, S., Ström, L., Tamstorf, M. P., & Christensen, T. R. (2008). Large tundra methane burst during onset of freezing. *Nature*, *456*(7222), 628–630. https://doi.org/10.1038/nature07464

McAfee, S. A., Guentchev, G., & Eischeid, J. K. (2013). Reconciling precipitation trends in Alaska: 1. Station-based analyses. *Journal of Geophysical Research: Atmospheres*, *118*(14), 7523–7541. https://doi.org/10.1002/jgrd.50572

McDermitt, D., Burba, G., Xu, L., Anderson, T., Komissarov, A., Riensche, B., et al. (2011). A new low-power, open-path instrument for measuring methane flux by eddy covariance. *Applied Physics B*, *102*(2), 391–405. https://doi.org/10.1007/s00340-010-4307-0

McGuire, A. D., Lawrence, D. M., Koven, C., Clein, J. S., Burke, E., Chen, G., et al. (2018). Dependence of the evolution of carbon dynamics in the northern permafrost region on the trajectory of climate change. *Proceedings of the National Academy of Sciences of the United States of America*, *115*(15), 3882–3887. https://doi.org/10.1073/pnas.1719903115

Michaelson, G. J., Ping, C. L., & Kimble, J. M. (1996). Carbon storage and distribution in tundra soils of Arctic Alaska, USA. *Arctic and Alpine Research*, *28*(4), 414–424. https://doi.org/10.2307/1551852

Moritz, R. E., Bitz, C. M., & Steig, E. J. (2002). Dynamics of recent climate change in the Arctic. *Science*, *297*(5586), 1497–1502. https://doi.org/10.1126/science.1076522

Muster, S., Langer, M., Heim, B., Westermann, S., & Boike, J. (2012). Subpixel heterogeneity of ice-wedge polygonal tundra: A multi-scale analysis of land cover and evapotranspiration in the Lena River Delta, Siberia. *Tellus B: Chemical and Physical Meteorology*, *64*(1), 17301. https://doi.org/10.3402/tellusb.v64i0.17301

National Oceanic and Atmospheric Administration. (2019). *Alaska had its hottest month on record in July*. Retrieved from https://www.noaa.gov/news/alaska-had-its-hottest-month-on-record-in-july

National Weather Service. (2019). *Alaska snow data*. National Oceanic and Atmospheric Administration. Retrieved from https://www.weather.gov/aprfc/Snow_Depth. Last

Nordstroem, C., Soegaard, H., Christensen, T. R., Friborg, T., & Hansen, B. U. (2001). Seasonal carbon dioxide balance and respiration of a high-Arctic fen ecosystem in NE-Greenland. *Theoretical and Applied Climatology*, *70*(1–4), 149–166. https://doi.org/10.1007/s007040170012

Norman, J. M., Kucharik, C. J., Gower, S. T., Baldocchi, D. D., Crill, P. M., Rayment, M., et al. (1997). A comparison of six methods for measuring soil-surface carbon dioxide fluxes. *Journal of Geophysical Research: Atmospheres*, *102*(D24), 28771–28777. https://doi.org/10.1029/97jd01440

Oechel, W. C., Hastings, S. J., Vourlrtis, G., Jenkins, M., Riechers, G., & Grulke, N. (1993). Recent change of Arctic tundra ecosystems from a net carbon dioxide sink to a source. *Nature*, *361*(6412), 520–523. https://doi.org/10.1038/361520a0

Oechel, W. C., Vourlitis, G. L., Hastings, S. J., & Bochkarev, S. A. (1995). Change in Arctic CO2 flux over two decades: Effects of climate change at Barrow, Alaska. *Ecological Applications*, *5*(3), 846–855. https://doi.org/10.2307/1941992

Ohmura, A. (1981). Climate and energy balance of the Arctic tundra, *Zürcher Geogr. Schr*, *3*, 448.

Ohmura, A. (1982). Climate and energy balance on the Arctic tundra. *Journal of Climatology*, *2*(1), 65–84. https://doi.org/10.1002/joc.3370020106

Olivas, P. C., Oberbauer, S. F., Tweedie, C., Oechel, W. C., Lin, D., & Kuchy, A. (2011). Effects of Fine-Scale Topography on CO_2 Flux Components of Alaskan Coastal Plain Tundra: Response to Contrasting Growing Seasons. *Arctic Antarctic and Alpine Research*, *43*(2), 256–266. https://doi.org/10.1657/1938-4246-43.2.256

Parmentier, F. J. W., Van Der Molen, M. K., Van Huissteden, J., Karsanaev, S. A., Kononov, A. V., Suzdalov, D. A., et al. (2011). Longer growing seasons do not increase net carbon uptake in the northeastern Siberian tundra. *Journal of Geophysical Research: Biogeosciences*, *116*(G4). https://doi.org/10.1029/2011jg001653

Pastorello, G., Gunter, D., Chu, H., Christianson, D., Trotta, C., Canfora, E., & Agarwal, D. (2017). Hunting data rogues at scale: Data quality control for observational data in research infrastructures. *Paper presented at the IEEE 13th International Conference on e-Science (e-Science)* 446–447. http://doi.org/10.1109/eScience.2017.64

Pastorello, G., Trotta, C., Canfora, E., Chu, H., Christianson, D., Cheah, Y. W., et al. (2020). The FLUXNET2015 dataset and the ONEFlux processing pipeline for eddy covariance data. *Scientific Data*, *7*(1), 1–27.

Pavelka, M., Acosta, M., Kiese, R., Altimir, N., Brümmer, C., Crill, P., et al. (2018). Standardisation of chamber technique for CO2, N2O and CH4 fluxes measurements from terrestrial ecosystems. *International Agrophysics*, *32*(4), 569–587.

Pirk, N., Santos, T., Gustafson, C., Johansson, A. J., Tufvesson, F., Parmentier, F. J. W., et al. (2015). Methane emission bursts from permafrost environments during autumn freeze-in: New insights from ground-penetrating radar. *Geophysical Research Letters*, *42*(16), 6732–6738. https://doi.org/10.1002/2015gl065034

Pirk, N., Sievers, J., Mertes, J., Parmentier, F. J. W., Mastepanov, M., & Christensen, T. R. (2017). Spatial variability of CO_2 uptake in polygonal tundra: Assessing low-frequency disturbances in eddy covariance flux estimates. *Biogeosciences*, *14*(12), 3157–3169. https://doi.org/10.5194/bg-14-3157-2017

Raz-Yaseef, N., Torn, M. S., Wu, Y., Billesbach, D. P., Liljedahl, A. K., Kneafsey, T. J., et al. (2017). Large CO_2 and CH_4 emissions from polygonal tundra during spring thaw in northern Alaska. *Geophysical Research Letters*, *44*(1), 504–513.

Reichstein, M., Falge, E., Baldocchi, D., Papale, D., Aubinet, M., Berbigier, P., et al. (2005). On the separation of net ecosystem exchange into assimilation and ecosystem respiration: Review and improved algorithm. *Global Change Biology*, *11*(9), 1424–1439. https://doi.org/10.1111/j.1365-2486.2005.001002.x

Rogers, A., Serbin, S. P., Ely, K. S., & Wullschleger, S. D. (2019). Terrestrial biosphere models may overestimate Arctic CO 2 assimilation if they do not account for decreased quantum yield and convexity at low temperature. *New Phytologist*, *223*(1), 167–179. https://doi.org/10.1111/nph.15750

Romanovsky, V., Cable, W., Dolgikh, K. (2017). Subsurface temperature, moisture, thermal conductivity and heat flux, barrow, A, B, C, D. In *Next generation ecosystem Experiments Arctic data collection [Data set]*. Oak Ridge National Laboratory, U.S. Department of Energy. https://doi.org/10.5440/1126515

Ruimy, A., Jarvis, P. G., Baldocchi, D. D., & Saugier, B. (1995). CO_2 fluxes over plant canopies and solar radiation: A review. *Advances in Ecological Research*, *26*, 1–68. https://doi.org/10.1016/s0065-2504(08)60063-x

Sachs, T., Giebels, M., Boike, J., & Kutzbach, L. (2010). Environmental controls on CH4 emission from polygonal tundra on the microsite scale in the Lena river delta, Siberia. *Global Change Biology*, *16*(11), 3096–3110. https://doi.org/10.1111/j.1365-2486.2010.02232.x

Sayres, D. S., Dobosy, R., Healy, C., Dumas, E., Kochendorfer, J., Munster, J., et al. (2017). Arctic regional methane fluxes by ecotope as derived using eddy covariance from a low-flying aircraft. *Atmospheric Chemistry and Physics*, *17*(13), 8619–8633. https://doi.org/10.5194/acp-17-8619-2017

Schotanus, P., Nieuwstadt, F. T. M., & De Bruin, H. A. R. (1983). Temperature measurement with a sonic anemometer and its application to heat and moisture fluxes. *Boundary-Layer Meteorology*, *26*(1), 81–93. https://doi.org/10.1007/bf00164332

Schuur, E. A., McGuire, A. D., Schädel, C., Grosse, G., Harden, J. W., Hayes, D. J., et al. (2015). Climate change and the permafrost carbon feedback. *Nature*, *520*(7546), 171–179. https://doi.org/10.1038/nature14338

Schuur, E. A., Vogel, J. G., Crummer, K. G., Lee, H., Sickman, J. O., & Osterkamp, T. E. (2009). The effect of permafrost thaw on old carbon release and net carbon exchange from tundra. *Nature*, *459*(7246), 556–559. https://doi.org/10.1038/nature08031

Sedighi, M., Hepburn, B. D. P., Thomas, H. R., & Vardon, P. J. (2018). Energy balance at the soil atmospheric interface. *Environmental Geotechnics*, *5*(3), 146–157. https://doi.org/10.1680/jenge.15.00054

Sen, P. K. (1968). Estimates of the regression coefficient based on Kendall's tau. *Journal of the American Statistical Association*, *63*(324), 1379–1389. https://doi.org/10.1080/01621459.1968.10480934

Shaver, G. R., Rastetter, E. B., Salmon, V., Street, L. E., van de Weg, M. J., Rocha, A., et al. (2013). Pan-Arctic modelling of net ecosystem exchange of CO2. *Philosophical Transactions of the Royal Society B: Biological Sciences*, *368*(1624), 20120485. https://doi.org/10.1098/rstb.2012.0485

Shiklomanov, N. I., Streletskiy, D. A., Nelson, F. E., Hollister, R. D., Romanovsky, V. E., Tweedie, C. E., et al. (2010). Decadal variations of active-layer thickness in moisture-controlled landscapes, Barrow, Alaska. *Journal of Geophysical Research: Biogeosciences*, *115*(G4). https://doi.org/10.1029/2009jg001248

Sloan, V., & Norby, R. (2014). Intensive site 1 vegetation plot photos, Barrow, Alaska, 2012. Next generation ecosystem experiments Arctic data collection [Data set]. Oak Ridge National Laboratory, U.S. Department of Energy. https://doi.org/10.5440/1177280

Song, C., Xu, X., Sun, X., Tian, H., Sun, L., Miao, Y, et al. (2012). Large methane emission upon spring thaw from natural wetlands in the northern permafrost region. *Environmental Research Letters*, *7*(3), 034009. https://doi.org/10.1088/1748-9326/7/3/034009

Streletskiy, D. A., Shiklomanov, N. I., Nelson, F. E. & Klene, A. E. (2008, June). Thirteen years of observations at Alaskan CALM sites: long-term active layer and ground surface temperature trends. In D. L. Kane, & K. M. Hinkel (Eds.), *Proceedings of the Ninth International Conference on Permafrost, Fairbanks, Alaska* (2, pp. 1727–1732). Institute of Northern Engineering, University of Alaska Fairbanks.

Sturtevant, C. S., & Oechel, W. C. (2013). Spatial variation in landscape-level CO2 and CH4 fluxes from Arctic coastal tundra: Influence from vegetation, wetness, and the thaw lake cycle. *Global Change Biology*, *19*(9), 2853–2866. https://doi.org/10.1111/gcb.12247

Svensson, H. (1963). Tundra polygons. Photographic interpretation and field studies in north Norwegian polygon areas. *Norges geologiske undersøkelse*, *223*, 298–327.

Tagesson, T., Mölder, M., Mastepanov, M., Sigsgaard, C., Tamstorf, M. P., Lund, M., et al. (2012). Land-atmosphere exchange of methane from soil thawing to soil freezing in a high-Arctic wet tundra ecosystem. *Global Change Biology*, *18*(6), 1928–1940. https://doi.org/10.1111/j.1365-2486.2012.02647.x

Taş, N., Prestat, E., Wang, S., Wu, Y., Ulrich, C., Kneafsey, T., et al. (2018). Landscape topography structures the soil microbiome in Arctic polygonal tundra. *Nature Communications*, *9*(1), 1–13.

Taylor, M. A., Celis, G., Ledman, J. D., Bracho, R., & Schuur, E. A. G. (2018). Methane efflux measured by eddy covariance in Alaskan upland tundra undergoing permafrost degradation. *Journal of Geophysical Research: Biogeosciences*, *123*(9), 2695–2710. https://doi.org/10.1029/2018jg004444

Torn, M. S., & Dengel, S. (2020). AmeriFlux US-NGB NGEE Arctic Barrow [Data set]. Lawrence Berkeley National Laboratory. https://doi.org/10.17190/AMF/1436326

Turetsky, M. R., Abbott, B. W., Jones, M. C., Anthony, K. W., Olefeldt, D., Schuur, E. A. G., et al. (2020). Carbon release through abrupt permafrost thaw. *Nature Geoscience*, *13*(2), 138–143. https://doi.org/10.1038/s41561-019-0526-0

Ueyama, M., Ichii, K., Iwata, H., Euskirchen, E. S., Zona, D., Rocha, A. V., et al. (2013). Upscaling terrestrial carbon dioxide fluxes in Alaska with satellite remote sensing and support vector regression. *Journal of Geophysical Research: Biogeosciences*, *118*(3), 1266–1281. https://doi.org/10.1002/jgrg.20095

Vaughn, L. J., Conrad, M. E., Bill, M., & Torn, M. S. (2016). Isotopic insights into methane production, oxidation, and emissions in Arctic polygon tundra. *Global Change Biology*, *22*(10), 3487–3502. https://doi.org/10.1111/gcb.13281

Vickers, D., & Mahrt, L. (1997). Quality control and flux sampling problems for tower and aircraft data. *Journal of Atmospheric and Oceanic Technology*, *14*(3), 512–526. https://doi.org/10.1175/1520-0426(1997)014<0512:qcafsp>2.0.co;2

Villarreal, S., Hollister, R. D., Johnson, D. R., Lara, M. J., Webber, P. J., & Tweedie, C. E. (2012). Tundra vegetation change near Barrow, Alaska (1972–2010). *Environmental Research Letters*, *7*(1), 015508. https://doi.org/10.1088/1748-9326/7/1/015508

von Fischer, J. C., Rhew, R. C., Ames, G. M., Fosdick, B. K., & von Fischer, P. E. (2010). Vegetation height and other controls of spatial variability in methane emissions from the Arctic coastal tundra at Barrow, Alaska. *Journal of Geophysical Research: Biogeosciences*, *115*(G4). https://doi.org/10.1029/2009jg001283

Vourlitis, G. L., Harazono, Y., Oechel, W. C., Yoshimoto, M., & Mano, M. (2000). Spatial and temporal variations in hectare-scale net CO2 flux, respiration and gross primary production of Arctic tundra ecosystems. *Functional Ecology*, *14*(2), 203–214. https://doi.org/10.1046/j.1365-2435.2000.00419.x

Wagner, D., Kobabe, S., Pfeiffer, E. M., & Hubberten, H. W. (2003). Microbial controls on methane fluxes from a polygonal tundra of the Lena Delta, Siberia. *Permafrost and Periglacial Processes*, *14*(2), 173–185. https://doi.org/10.1002/ppp.443

Wainwright, H. M., Dafflon, B., Smith, L. J., Hahn, M. S., Curtis, J. B., Wu, Y., et al. (2015). Identifying multiscale zonation and assessing the relative importance of polygon geomorphology on carbon fluxes in an Arctic tundra ecosystem. *Journal of Geophysical Research: Biogeosciences*, *120*(4), 788–808. https://doi.org/10.1002/2014jg002799

Wainwright, H. M., Liljedahl, A. K., Dafflon, B., Ulrich, C., Peterson, J. E., Gusmeroli, A., & Hubbard, S. S. (2017). Mapping snow depth within a tundra ecosystem using multiscale observations and Bayesian methods. *The Cryosphere*, *11*(2), 857–875. https://doi.org/10.5194/tc-11-857-2017

Wang, F., Shao, W., Yu, H., Kan, G., He, X., Zhang, D., et al. (2020). Re-evaluation of the power of the Mann-Kendall test for detecting monotonic trends in hydrometeorological time series. *Frontiers of Earth Science*, *8*. https://doi.org/10.3389/feart.2020.00014

Webb, E. K., Pearman, G. I., & Leuning, R. (1980). Correction of flux measurements for density effects due to heat and water vapour transfer. *Quarterly Journal of the Royal Meteorological Society*, *106*(447), 85–100. https://doi.org/10.1002/qj.49710644707

Webber, P. J. (1978). Spatial and temporal variation of the vegetation and its production, Barrow, Alaska. In Tieszen, L. L. (Ed.), *Vegetation and production ecology of an Alaskan Arctic tundra. Ecological Studies (Analysis and Synthesis)*, (Vol. 29, pp. 37–112). Springer. https://doi.org/10.1007/978-1-4612-6307-4_3

Wendler, G., Gordon, T., & Stuefer, M. (2017). On the precipitation and precipitation change in Alaska. *Atmosphere*, *8*(12), 253. https://doi.org/10.3390/atmos8120253

Wilkman, E., Zona, D., Tang, Y., Gioli, B., Lipson, D. A., & Oechel, W. (2018). Temperature response of respiration across the heterogeneous landscape of the Alaskan Arctic tundra. *Journal of Geophysical Research: Biogeosciences*, *123*(7), 2287–2302. https://doi.org/10.1029/2017jg004227

Wille, C., Kutzbach, L., Sachs, T., Wagner, D., & Pfeiffer, E. M. (2008). Methane emission from Siberian Arctic polygonal tundra: Eddy covariance measurements and modeling. *Global Change Biology*, *14*(6), 1395–1408. https://doi.org/10.1111/j.1365-2486.2008.01586.x

Wilson, C., & Altmann, G. (2017). Digital elevation model, 0.25 m, Barrow Environmental Observatory, Alaska, 2013. Next generation ecosystem Experiments Arctic data collection [Data set]. Oak Ridge National Laboratory, U.S. Department of Energy. https://doi.org/10.5440/1224720

Wohlfahrt, G., & Galvagno, M. (2017). Revisiting the choice of the driving temperature for eddy covariance CO2 flux partitioning. *Agricultural and Forest Meteorology*, *237*, 135–142. https://doi.org/10.1016/j.agrformet.2017.02.012

Yi, Y., Kimball, J. S., Chen, R. H., Moghaddam, M., Reichle, R. H., Mishra, U., et al. (2018). Characterizing permafrost active layer dynamics and sensitivity to landscape spatial heterogeneity in Alaska. *The Cryosphere*, *12*(1), 145–161. https://doi.org/10.5194/tc-12-145-2018

Zamolodchikov, D. G., Karelin, D. V., Ivaschenko, A. I., Oechel, W. C., & Hastings, S. J. (2003). CO_2 flux measurements in Russian Far East tundra using eddy covariance and closed chamber techniques. *Tellus B*, *55*(4), 879–892. https://doi.org/10.1046/j.1435-6935.2003.00074.x

Zhang, Y., Chen, W., Smith, S. L., Riseborough, D. W., & Cihlar, J. (2005). Soil temperature in Canada during the twentieth century: Complex responses to atmospheric climate change. *Journal of Geophysical Research*, *110*(D3). https://doi.org/10.1029/2004jd004910

Zhang, Y., Sachs, T., Li, C., & Boike, J. (2012). Upscaling methane fluxes from closed chambers to eddy covariance based on a permafrost biogeochemistry integrated model. *Global Change Biology*, *18*(4), 1428–1440. https://doi.org/10.1111/j.1365-2486.2011.02587.x

Zona, D., Gioli, B., Commane, R., Lindaas, J., Wofsy, S. C., Miller, C. E., et al. (2016). Cold season emissions dominate the Arctic tundra methane budget. *Proceedings of the National Academy of Sciences of the United States of America*, *113*(1), 40–45. https://doi.org/10.1073/pnas.1516017113

Zona, D., Lipson, D. A., Zulueta, R. C., Oberbauer, S. F., & Oechel, W. C. (2011). Microtopographic controls on ecosystem functioning in the Arctic Coastal Plain. *Journal of Geophysical Research: Biogeosciences*, *116*(G4). https://doi.org/10.1029/2009jg001241

Zona, D., Oechel, W. C., Kochendorfer, J., Paw, U. K. T., Salyuk, A. N., Olivas, P. C., et al. (2009). Methane fluxes during the initiation of a large-scale water table manipulation experiment in the Alaskan Arctic tundra. *Global Biogeochemical Cycles*, *23*(2). https://doi.org/10.1029/2009gb003487

Zona, D., Oechel, W. C., Peterson, K. M., Clements, R. J., Paw, U. K. T., & Ustin, S. L. (2009). Characterization of the carbon fluxes of a vegetated drained lake basin chronosequence on the Alaskan Arctic Coastal Plain. *Global Change Biology*, *16*(6), 1870–1882. https://doi.org/10.1111/j.1365-2486.2009.02107.x